Hybrid Intelligent Control Using Hippocampus-Based Fuzzy Neural Networks for Active Power Filter

Shixi Hou, *Member, IEEE*, Zhenyu Qiu, Yundi Chu, Jie Gao, and Juntao Fei, *Senior Member, IEEE*

***Abstract*—To tackle harmonic issue in the power grid, an intelligent control scheme consists of fast integral terminal sliding-mode control and hippocampus-based fuzzy neural network (HBFNN) is proposed and applied to active power filter (APF) to eliminate harmonics in this article. At first, the mathematical model of APF under the influence of external interference and parameter perturbation is derived in accordance with its topological structure. Afterwards, a fast integral terminal sliding-mode controller is developed for APF. The system stability is subsequently proved according to Lyapunov stability criterion, and the finite-time convergence of tracking error is certified. In addition, based on the biological structure and characteristics of the hippocampus, an innovative HBFNN is constructed to approximate the controller. Furthermore, the adaptive laws derived by the Lyapunov's theorem can realize the automatic adjustment of parameters and ensure closed-loop stability. Ultimately, relevant simulation and experimental results corroborate the availability and superiority of the designed intelligent control strategy in harmonic elimination.**

***Index Terms*—Active power filter (APF), fast integral terminal sliding-mode control (FITSMC), fuzzy neural network (FNN), hippocampus.**

NOMENCLATURE

Variables

i_s	Source current.
i_L	Load current.
i_c	Compensation current.
i_h	Reference compensation current.
U_s	Source voltage.
U_{dc}	DC-link capacitor voltage.
R	Equivalent resistance.
L	Inductance.
C	DC-link capacitor.
U_{dc}^*	Reference dc-link capacitor voltage.
R_1,R_2,R_3,R_4	Resistance of the nonlinear load.
C_{L1},C_{L2}	Capacitors of the nonlinear load.
S_1,S_2,S_3,S_4	Conduction state of the insulate-gate bipolar transistor (IGBT).
R_n	Nominal value of R.
L_n	Nominal value of L.
H	Lumped uncertainties caused by external disturbance and internal parameter perturbation.
e	Tracking error of compensation current.
s	Sliding surface.
u_{eq}	Equivalent control law.
u_c	Robust control law.
$\text{sgn}(s)$	Sign function.
u_{FITSMC}	Control law of designed fast integral terminal sliding-mode control (FITSMC).
V,V_r	Lyapunov function.
W,W_h,W_r,W_f	Weights of hippocampus-based fuzzy neural network (HBFNN).
σ,μ,b_l,b_r,c,ϕ,θ,Φ,$\hat{\delta}_d$	Variables of HBFNN.
u_{com}	Adaptive compensation term.

Parameters

H_M	Upper bound of H.
α,β,p,q	Parameters of sliding surface.
η,ε	Parameters of robust control law.
κ, τ	Parameters of Lemma 1.
$\text{sat}(s)$	Saturation function.
Ω	Thickness of the boundary layer.
m	Number of nodes in the input layer.
n	Number of nodes in the membership layer.
v	Number of nodes in the hippocampus layer.
z	Number of nodes in the rule layer.
D_t	Predesigned threshold value of DG layer.
f	Supply frequency.
f_{sw}	Switching frequency.
$\eta_1, \ldots, \eta_{13}$	Learning rates of HBFNN.

Received 22 March 2024; revised 14 June 2024 and 26 July 2024; accepted 10 August 2024. Date of publication 23 August 2024; date of current version 7 October 2024. This work was supported by the National Natural Science Foundation of China under Grant 62103132 and Grant 62003132, in part by the Major Special Science and Technology Project of Yunnan Province under Grant 202402AF080006, and in part by the Changzhou Sci&Tech Program under Grant CJ20230041. Recommended for publication by Associate Editor B. Singh. *(Corresponding author: Shixi Hou.)*

The authors are with the College of Artificial Intelligence and Automation and Jiangsu Key Laboratory of Power Transmission and Distribution Equipment Technology, Hohai University, Nanjing 210098, China (e-mail: houshixi@hhu.edu.cn; 221320020004@hhu.edu.cn; 20191011@hhu.edu.cn; 221620010012@hhu.edu.cn; johnfei123@163.com).

Color versions of one or more figures in this article are available at https://doi.org/10.1109/TPEL.2024.3449043.

Digital Object Identifier 10.1109/TPEL.2024.3449043

Index

THD	Total harmonic distortion.
ET	Execution time.
RMSE	Root mean squared error.

I. Introduction

A. Background

With the ever-increasing number of nonlinear loads connected to the power grid, harmonic problems have become increasingly severe, which will cause the damage of power equipment and the deterioration of power quality, so how to eliminate harmonics has been considerably concerned by researchers. Through the efforts of relevant scholars, the existing research has recognized the crucial role played by active power filter (APF) in harmonic elimination, which is an effective device to suppress load harmonics by proactively generating reverse harmonics [1], [2], [3], [4], [5].

As one of the most important parts in APF, current tracking control will affect the effect of harmonic elimination to a large extent. With the more intensive research of researchers, the application of APF is becoming more and more mature, and plenty of excellent current tracking control methods have emerged, such as proportional integral (PI) control [6], proportional resonance control [7], repetitive control [8], sliding-mode control (SMC) [9], and so on. Throughout these control methods, the most representative and effective one is the SMC, which is the focus of recent research. Compared with other control methods (e.g., PI control [6], proportional resonance control [7], repetitive control [8]), SMC can address nonlinear control problems well, even in the presence of interference, and is distinguished for its high precision and strong robustness, which is perfectly applicable to APF [10], [11], [12], [13]. However, the original SMC has a fatal defect, that is, the tracking error cannot converge to zero in a finite time, which makes it arduous to obtain satisfactory control accuracy [14], [15].

B. Related Works

To remedy the deficiency mentioned above, a terminal sliding-mode control (TSMC) that possesses the property of finite-time convergence has been developed. It has successfully replaced the traditional SMC and is extensively adopted in nonlinear systems to achieve higher control accuracy [16], [17]. Wang et al. [18] designed a TSMC scheme for flexible-joint robots with unknown disturbance to achieve the purpose of tracking their trajectory. The results indicate that this method has achieved the expected control effect, exhibiting strong robustness while also possessing finite-time convergence. Despite the TSMC can iron out the problem that tracking error cannot converge in a finite time, the convergence speed is still not satisfactory. In a bid to shorten the convergence time and pursue a better dynamic performance, a fast terminal sliding-mode control (FTSMC) has been proposed, which can provide both finite-time convergence property and fast convergence performance, so it is more appropriate in industrial applications [19], [20]. For instance, for permanent magnet motor, Kumar et al. [21] adopted a continuous FTSMC with a view to realizing precise speed control. The experimental results and analysis reveal that the utilized FTSMC can make the tracking error rapidly converge in a limited time and still maintain an excellent performance. Nevertheless, except for the abovementioned problems related to the error convergence of SMC, there also exists a nonglobal robustness issue that needs to be settled urgently owing to the existence of the reaching phase in the control process, which has a significant impact on the control effect. To tackle this issue, an integral sliding-mode control (ISMC) has been proposed. In virtue of the existence of integral terms, the system state is initially on the sliding surface, which can skip the reaching phase and ensure the robustness of the disturbed system at the very start. There have been a great quantity of intensive studies involving ISMC that have validated its global robustness in nonlinear systems [22], [23], [24]. In [25] and [26], two different ISMC schemes were used in perturbed motor systems and mobile robots, respectively, and the respective results manifest that ISMC is insensitive to disturbance and has superior control performance, besides, it also possesses strong robustness throughout the whole control process. Inspired by the abovementioned analyzes, a fast integral terminal sliding-mode control (FITSMC) method that comprises the merits of FTSMC and ISMC is proposed for APF in this article. As envisaged, the proposed FITSMC not only enables the errors to converge quickly in a finite time, but also ensures the global robustness. However, a crucial prerequisite for the designed FITSMC to achieve accurate control is whether the relevant prior knowledge is precise. Given the complex dynamic environment and the unknown parameter perturbation in the industrial field, it is difficult to obtain accurate values [27]. Thus, the designed controller will fail to achieve the expected control performance.

To get out of the abovementioned scrape, some researchers have adopted a hybrid intelligent control algorithm that combines SMC and neural networks (NNs). Owing to the universal approximation theory of NN, it can be used to approximate the unknown part of the designed controller. Numerous investigators have examined the effects of NN on uncertainty approximation and have drawn the conclusion that NN possesses accurate approximation ability [28], [29]. Fei et al. [30] designed a control scheme combining fractional-order sliding-mode control and recurrent neural network (RNN) and utilizes RNN to estimate the unknown function in the controlled system, which effectively improves the control accuracy of the system. The past few decades have witnessed the rapid development of NN in control filed. Due to its foreseeable broad application prospects, it has become a research hotspot at present.

Recently, brain-like NNs based on some specific neural structures in the human brain has been proposed to achieve information processing, and subsequently have received considerable attention. One of the most representative is the emotional neural network (ENN), which is structured in accordance with the brain's emotional learning mechanisms. Relevant literature has validated its excellent dynamic performance through experimental results [31], [32]. Zhang et al. [33] proposed a novel ENN based on artificial NN, which possess higher efficiency than conventional NNs on recognizing digit. Nevertheless, brain-like

NNs such as ENN are unable to distinguish the importance of input signals, leading to the inability to store valid information and delete invalid information, which affect the learning speed and network performance. For this reason, it is necessary to develop a new brain-like NN that can address the abovementioned issues. The hippocampus, which now frequently appears in the study of biological brains, seems to offer an entirely new idea. The hippocampus refers to a key structure located inside the brain that plays an important role in learning and memory. It transmits and integrates information through complex NN connections. After a long and extensive study, scholars have found that the hippocampus is involved in the formation, storage and deletion of associative memories in the brain [34], [35], [36]. According to this feature and its biological structure, a new brain-like intelligent NN based on the hippocampus is developed in this article.

In addition, due to the strong reasoning capability of fuzzy logic system, the fuzzy neural networks (FNN), which integrates NN with fuzzy logic theory, has also gained much attention [37], [38]. For instance, Lin et al. [39] presented a new FNN combining ENN and fuzzy logic for information encryption and decryption. It can be seen from two simulation examples that the proposed FNN possesses superior approximation effectiveness. Thus, it is a reliable way to combine the hippocampus NN with fuzzy logic to improve its approximation performance.

C. Contribution and Article Organization

Deeply illuminated by the abovementioned discussion, an innovative hippocampus-based fuzzy neural network (HBFNN) is proposed to approximate the designed FITSMC for APF. Compared with the existing literature, the main contributions and innovations of this article are as follows.

1) A novel FITSMC scheme is designed for APF to compensate harmonic current. The designed FITSMC possesses the properties, such as high precision, fast response, and finite-time convergence. Besides, according to the Lyapunov stability criterion, the stability of the closed-loop system has been strictly proved.
2) An original HBFNN is proposed to approximate the uncertainties of the designed controller to achieve a better control performance. Compared with ordinary NN, the proposed HBFNN can filter the input information according to its importance, thereby reducing the computation burden and improving the learning speed.
3) The HBFNN innovatively adopts the activation function with feature selection effect to realize the transmission of important signals and the deletion of nonimportant signals, so as to simulate the mechanism of hippocampus. In addition, unlike the long short-term memory network (LSTM), HBFNN is derived from the biological structure, and is closer to the form of biological NN. Besides, owing to its unique double recurrent structure, it can effectively deal with time-varying signals, and has stronger anti-interference performance than RNN.
4) For all we know, this is the first time to completely create a new FNN based on the structure and characteristics of the hippocampus and combine it with FITSMC to form a new control scheme applied for APF. The stability of the closed- loop system is also proved by the Lyapunov stability theorem. Furthermore, a series of simulation and experimental results validate the effectiveness and superiority of the proposed control scheme from many aspects.

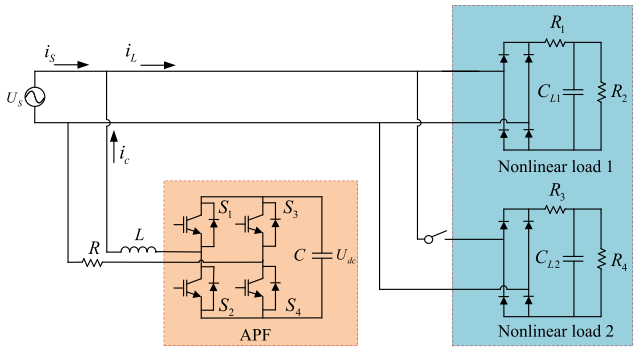

Fig. 1. Single-phase APF.

The rest of this article is organized as follows. In Section II, the APF mathematical model is given, then the FITSMC is designed for APF, and system stability and error finite-time convergence are proved. In Section III, the HBFNN is constructed and is introduced in detail. Section IV adopts HBFNN to approximate the controller and designs the adaptive laws to ensure that the system is stable. In Section V, various software simulation and hardware experiments are carried out to demonstrate the effectiveness of the proposed scheme for APF. Finally, Section VI concludes this article.

Remark 1: This article proposes a hybrid control method that bridges the research gap between the feature selection mechanism, ENN, FITSMC, double recurrent structure and parameter adaptive adjustment successfully for the first time, and explores the efficient and reliable connection mechanism between these independent control techniques, making the system have an excellent tracking performance and generalization ability. The designed FITSMC ensures that the tracking error of the system can converge to zero in a finite time. Generally, only by grasping the specific model information of the controlled object can the SMC exert good performance. However, due to external disturbances and the burn-in of equipment, it is difficult for us to accurately calculate the specific values of the model parameters, which will make the control accuracy of the system decrease [28], [30]. Therefore, we design a novel HBFNN to learn the original SMC, which overcomes the adverse effect of uncertainties and significantly improves the control accuracy.

II. Problem Formulation

To derive the mathematical model of single-phase APF subjected to disturbances, the diagram of APF is shown in Fig. 1, where the symbols $i_s, i_L, i_c, U_s, U_{\rm dc}, R, L, C$ denote source current, load current, compensation current, source voltage, dc-link capacitor voltage, equivalent resistance, inductance, dc-link capacitor, respectively. $U_{\rm dc}^*$ is the reference voltage of dc-link

capacitor and $U_{\text{dc}}^{*} = 50$ V. R_1,R_2,R_3,R_4,C_{L1}, and C_{L2} are the resistance and capacitors of the nonlinear load, respectively. S_1,S_2,S_3, and S_4 represent the ON–OFF state of the insulate-gate bipolar transistor (IGBT). Then, the mathematical expression can be derived as follows [40]:

$$\ddot{i}_c = f(i_c) + \psi u + H \tag{1}$$

where $f(i_c) = \frac{R_n^2}{L_n^2} i_c - \frac{R_n}{L_n^2} U_s + \frac{1}{L_n} \dot{U}_s$, $\psi = \frac{R_n}{L_n^2} U_{\text{dc}} - \frac{1}{L_n} \dot{U}_{\text{dc}}$, R_n is the nominal value of R, L_n is the nominal value of L, and u represents switching state. Since the control frequency of the current loop is much higher than that of the voltage loop, U_{dc} can be regarded as a positive constant when designing the current loop, that is, $\dot{U}_{\text{dc}} = 0$. Thus, ψ can be considered as a positive constant in (1). H is the lumped uncertainties caused by external disturbance and internal parameter perturbation. It is assumed that H has an upper bound H_M, which satisfies $|H| \le H_M$, where H_M is a positive constant.

Define the tracking error as

$$e = i_c - i_h \tag{2}$$

where i_h is the reference signal for compensation current.

Hence, the first derivative of e could be denoted as

$$\dot{e} = \dot{i}_c - \dot{i}_h. \tag{3}$$

The fast integral terminal sliding surface designed in this article can be formulated as

$$s = \dot{e} + \alpha e + \beta \int_0^t e^{p/q} d\tau \tag{4}$$

where α and β both are gain parameters. To ensure the stable operation, α and β must be greater than zero [42], [10], [12]. p and q are both positive odd constants and $p < q$.

Taking the derivative of s yields

$$\begin{aligned} \dot{s} &= \ddot{e} + \alpha \dot{e} + \beta e^{p/q} \\ &= \ddot{i}_c - \ddot{i}_h + \alpha \dot{e} + \beta e^{p/q} \\ &= f(i_c) + \psi u + H - \ddot{i}_h + \alpha \dot{e} + \beta e^{p/q}. \end{aligned} \tag{5}$$

Design the control law as

$$u_{\text{FITSMC}} = u_{\text{eq}} + u_c. \tag{6}$$

When $H = 0$ and $\dot{s} = 0$, the equivalent control term u_{eq} can be obtained and expressed as [30], [43]

$$u_{\text{eq}} = \psi^{-1}(\ddot{i}_h - f(i_c) - \alpha \dot{e} - \beta e^{p/q}). \tag{7}$$

Then, design the following robust control term:

$$u_c = -\psi^{-1} \eta \text{sgn}(s) \tag{8}$$

where η is a positive constant slightly greater than the value of H_M. To facilitate the analysis, denote η as $\eta = H_M + \varepsilon$, where ε is infinitesimal and $\varepsilon > 0$. And $\text{sgn}(s)$ is a sign function whose standard form is

$$\text{sgn}(s) = \begin{cases} 1 & s > 0 \\ 0 & s = 0 \\ -1 & s < 0 \end{cases}. \tag{9}$$

Therefore, the FITSMC can ultimately be written as

$$\begin{aligned} u_{\text{FITSMC}} &= u_{\text{eq}} + u_c \\ &= \psi^{-1} \left[\ddot{i}_h - f(i_c) - \alpha \dot{e} - \beta e^{p/q} - \eta \text{sgn}(s) \right]. \end{aligned} \tag{10}$$

Proof: Choose the Lyapunov function as

$$V = \frac{1}{2} s^2. \tag{11}$$

Taking the derivative of $V$and substituting (5) and (10) into (11) yields

$$\begin{aligned} \dot{V} &= s\dot{s} \\ &= s\left[H - \eta \ \text{sgn}(s)\right] \\ &\le (H_M - H_M - \varepsilon)|s| = -\varepsilon |s| \\ &\le 0. \end{aligned} \tag{12}$$

On this basis, the inequality $\int_0^t \dot{V} dt < -\varepsilon \int_0^t |s| dt$ can be further obtained, then one can get that $\int_0^t |s| dt < \frac{V(0) - V(t)}{\varepsilon}$. Since $V(0)$ is bounded, $V(t)$ is bounded and decreasing, so $\int_0^t |s| dt$ is also bounded. And by referring to the Barbalat's lemma, we can get $\lim_{t \to \infty} s(t) = 0$, then e and $\dot{e}$ will be converged to zero. Consequently, the closed-loop stability can be guaranteed.

Next, before proving the error convergence, introduce the following lemma.

Lemma 1 [44]: Providing that there exists a positive definite Lyapunov function $V(x)$, which satisfies the following inequality:

$$\dot{V}(x) + \kappa V^{\tau}(x) \le 0 \tag{13}$$

where$x \in R, \kappa > 0, 0 < \tau < 1$. For any initial condition $V(x(0)) = V(0)$, $V(x)$ can converge to equilibrium point in finite time and the convergence time t_r meets the following inequality:

$$t_r \le \frac{1}{\kappa(1-\tau)} V^{1-\tau}(0). \tag{14}$$

Subsequently, combining (12) with Lemma 1 yields

$$t_{\text{rFITSMC}} \le \frac{\sqrt{2}}{\varepsilon} V^{\frac{1}{2}}(0). \tag{15}$$

According to the abovementioned analysis, one conclusion can be drawn that FITSMC can ensure the system stability and make the track error converge to zero in a finite time.

Remark 2: Despite the excellent dynamic performance of FITSMC, there is still an inevitable chattering phenomenon due to sliding-mode variable repeatedly passing through the surface caused by the discontinuous switching function, which have a serious impact on the control effect. Hence, in a bid to alleviate the chattering problem of FITSMC, the following saturation function can be adopted to replace the sign function in (9) by referring to the most common boundary layer method [45]:

$$\text{sat}(s) = \begin{cases} 1 & s > \Omega \\ \frac{1}{\Omega} s & -\Omega \le s \le \Omega \\ -1 & s < -\Omega \end{cases} \tag{16}$$

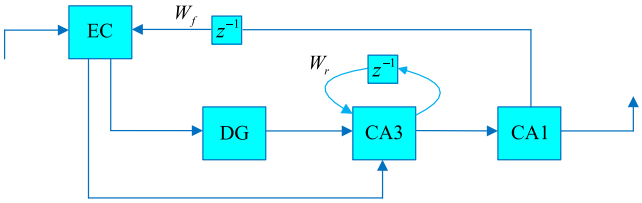

Fig. 2. Structure of hippocampus tissue in the human brain.

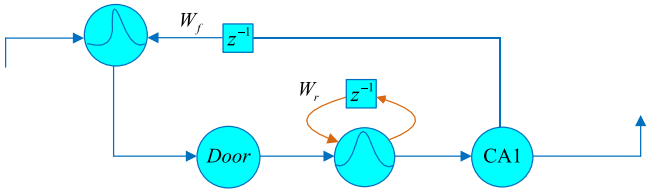

Fig. 3. Modified structure of hippocampus.

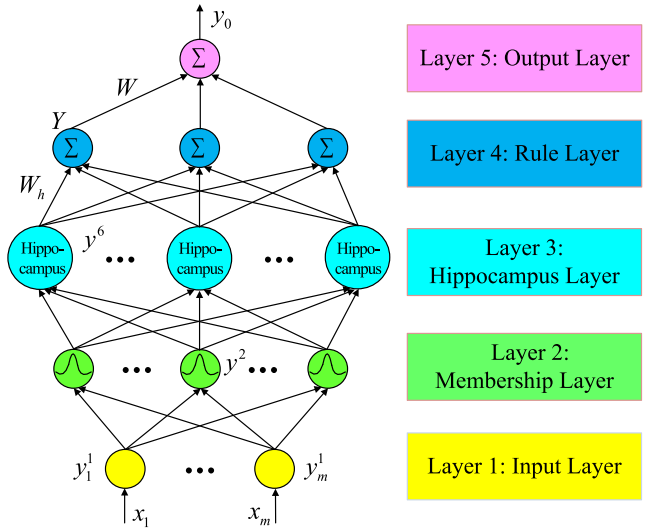

Fig. 4. Structure of HBFNN.

where Ω is the thickness of the boundary layer, and it is a positive constant. If Ω is too small, the chattering will not be suppressed effectively. If Ω is too large, the steady-state error of the system may increase [46]. Therefore, using the trail-and-error method, we choose: $\Omega = 0.5$.

III. Proposed HBFNN

To approximate the uncertainties in the FITSMC designed in the previous section, an innovative HBFNN is proposed and constructed in this section.

First, as shown in Fig. 2, the model diagram of the hippocampus is obtained according to reference [36], which contains entorhinal cortex (EC), dentate gyrus (DG), cornu ammonis 1 (CA1) and cornu ammonis 3 (CA3). Meanwhile, refer to Baghbani et al.'s practice of deleting the direct connection between the thalamus and the amygdala in ENN in [31] to improve the network performance, the information transmission structure of the hippocampus is adjusted here, that is, the direct connection between EC and CA3 is deleted to prevent interference with the learning process and reduce computation. The modified structure of the hippocampus is depicted in Fig. 3. Finally, it is combined with FNN to form the specific HBFNN, which structure diagram is presented in Fig. 4. There are five layers in the proposed HBFNN, which are input layer, membership layer, hippocampus layer, rule layer, and output layer, respectively. The specific expressions of each layer of the HBFNN are shown in (17)–(30):

Layer 1: Input layer: There are m nodes in this layer, and the input and output of the ith node in this layer can be written as

$$\text{net}_i^1(N) = x_i, i = 1, \ldots, m \tag{17}$$

$$y_i^1(N) = g^1\left(\text{net}_i^1(N)\right) = \text{net}_i^1(N) \tag{18}$$

where x_i is the ith input signal and $y_i^1(N)$ is the output signal of the input layer.

Layer 2: Membership layer: In this layer, the Gaussian functions are utilized as the activation functions to realize the fuzzification processing. There are n nodes, and the input and output of nodes in this layer are defined as

$$net_j^2(N) = -\sum_{i=1}^{m} \frac{\left(x_i^2(N) - \mu_{ji}\right)^2}{\sigma_{ji}^2} \tag{19}$$

$$y_j^2(N) = \exp(\text{net}_j^2(N)) \tag{20}$$

where $j = 1, 2, \ldots, n$, $x_i^2(N) = y_i^1(N)$, μ and σ represent the center and base width of the Gaussian function, respectively.

Layer 3: Hippocampus layer: In this layer, there are v hippocampus. First, the EC processes the received signals, where the asymmetric Gaussian function is adopted as activation function. Compared with the standard symmetric Gaussian function, the asymmetric Gaussian function can segment the input space more efficiently, besides, it has higher variability and flexibility. Consequently, it can make the network enhance the approximation precision and improve the learning ability [47]. And the output of EC and the asymmetric Gaussian function can be formulated as

$$net_g^3(N) = -\sum_{j=1}^{n} \frac{\left(x_j^3(N) - c_{gj}\right)^2}{b_{gj}^2} \tag{21}$$

$$y_g^3(N) = \exp(\text{net}_g^3(N)) * (w_{fg} * y_g^6(N-1)) \tag{22}$$

$$\frac{\left(x_j^3(N) - c_{gj}\right)^2}{b_{gj}^2} = \begin{cases} \frac{\left(x_j^3(N) - c_{gj}\right)^2}{\left(b_{lgj}\right)^2}, & -\infty < x_j^3(N) \le c_{gj} \\ \frac{\left(x_j^3(N) - c_{gj}\right)^2}{\left(b_{rgj}\right)^2}, & c_{gj} < x_j^3(N) < \infty \end{cases} \tag{23}$$

where $g = 1, 2, \ldots, v$, c,b_l, and b_r represent the mean, left-side, and right-side standard deviations of asymmetric Gaussian function, $y_g^3(N)$ is the output signal of the EC, w_f is the recurrent weight, and $y_g^6(N-1)$ is the previous output of CA1.

Then, the DG receives the output signals from the EC, and it plays a role of gating control. Here, we introduce the index of feature degree, which is the exact index to measure the importance of the signal. Through the specific feature selection algorithm, effective features in the information can be extracted and the unfavorable features can be removed, which can alleviate the computing burden and improve the network performance. The specific form of the feature degree and the output of DG are given as

$$\varphi_g(N) = (1 - \exp(-\phi_g(N)) \tag{24}$$

$$y_g^4(N) = \begin{cases} 0 & \varphi_g(N) \le D_t \\ y_g^3(N) * (1 - \exp(-\phi_g(N)) & \varphi_g(N) > D_t \end{cases} \tag{25}$$

where D_t is the predesigned threshold value, which satisfies $0 < D_t < 1$, and it is often designed as a constant to simplify implementation in practical application. $\phi_g(N)$ is the feature degree of the gth node, $\varphi_g(N)$ is the door adjuster, and $y_g^4(N)$ is the output of DG after being processed by the feature selection mechanism. According to the abovementioned expression, it can be found that if $\varphi_g(N) = 1$, the output of DG is exactly equal to the input, which manifests that the input information is completely valid; if $D_t < \varphi_g(N) < 1$, the output of DG is equal to the input multiplied by $\varphi_g(N)$, which means that the input information is filtered, the useful information is passed on, and the unfavorable information is removed; conversely, if $\varphi_g(N) \le D_t$, the output of DG is 0, which means that any information does not be transmitted.

Subsequently CA3 accepts the input signals after being filtered by DG and utilizes Gaussian function as activation function. The output of CA3 can be expressed as

$$net_g^5(N) = -\frac{\left(x_g^5(N) + w_{rg} * y_g^5(N-1) - \Phi_g\right)^2}{\theta_l^2} \tag{26}$$

$$y_g^5(N) = \exp(net_g^5(N)) \tag{27}$$

where $x_g^5(N) = y_g^4(N)$, Φ and θ are the center and base width of the Gaussian function, w_r is the recurrent weight, and $y_g^5(N-1)$ is the previous output of CA3.

Finally, the output signals from CA3 are transmitted to CA1. Referring to biological literature, since the cells related to memory formation mainly exist in EC and CA3, it makes sense that CA1 only plays a role in transmitting signals here without any processing of the signals. Consequently, the final output after processing by the hippocampus can be written as

$$y_g^6(N) = y_g^5(N). \tag{28}$$

At this point, the introduction of the hippocampus layer is complete. According to the abovementioned analysis, the combination of EC and DG realizes information filtering through the extraction of information features, which outputs useful information and removes unimportant information to reduce computation. It successfully simulates memory storage, i.e., transmission of important memories and deletion of useless memories. Despite LSTM's deletion gate has a similar function, it simulates the circuit structure, while the hippocampus simulates the biological brain structure, which is closer to the real NN. Besides, the structure of the hippocampus layer is more concise with fewer parameters. Meanwhile, compared with traditional RNN, it has a distinctive double recurrent structure, which can effectively process time-varying input signals and possesses stronger robustness. In conclusion, the hippocampus layer comprises the virtues of LSTM and RNN, it not only can filter information, but also has a faster learning speed and extreme insensitivity to disturbance.

Layer 4: Rule layer: There are z nodes in the rule layer, and the output of nodes in this layer is given as

$$y_l(N) = \sum_{g=1}^{v} y_g^6(N) w_{hlg} \tag{29}$$

where $l = 1, 2, \ldots, z$, w_h is the connective weight between the hippocampus layer and the rule layer.

Layer 5: Output layer: There is one output node in this layer, which is formulated as

$$y_o(N) = \sum_{l=1}^{z} y_l(N) w_l \tag{30}$$

where $y_o(N)$ is the output of the proposed HBFNN and w is the connective weight between the rule layer and the output layer.

IV. Proposed Hybrid Control Algorithm

The control performance of FITSMC designed in the previous section relies mightily on the accuracy of prior knowledge. However, owing to the existence of uncertainties stemmed from external interference and internal parameter perturbation, its control accuracy is seriously affected. To settle this issue and enhance the control performance, it is feasible and effective to approximate u_{FITSMC} by using the proposed HBFNN, which has more superior characteristics than the conventional NN.

First, according to the structure of HBFNN, the ideal value of the designed controller u_{FITSMC} can be written as $u_{\text{FITSMC}} = W^{*T} Y^* + \varepsilon_0$, where $W^*$is ideal value of the weight W, Y^* is the ideal output of the rule layer, and the reconstruction error ε_0 satisfies $|\varepsilon_0| \le \varepsilon_r$. Accordingly, the actual value of the controller approximated by HBFNN can be formulated as $u_{\text{HBFNN}} = \hat{W}^T \hat{Y}$, where u_{HBFNN} is the output of HBFNN, $\hat{W}$ and $\hat{Y}$ represent the estimates of W^* and Y^*, respectively. $\hat{W} = [w_1, w_2, \ldots, w_z]^T$, and $\hat{Y} = [y_1, y_2, \ldots, y_z]^T$. Meanwhile, to facilitate the analysis, $\hat{Y}$ can be denoted as $\hat{Y} = \hat{Y}(x, \sigma, \mu, b_l, b_r, c, \phi, \theta, \Phi, W_f, W_r, W_h)$, where $\sigma = [\sigma_{11}, \ldots, \sigma_{1m}, \sigma_{21}, \ldots, \sigma_{2m}, \ldots, \sigma_{n1}, \ldots, \sigma_{nm}]^T$, $\mu = [\mu_{11}, \ldots, \mu_{1m}, \mu_{21}, \ldots, \mu_{2m}, \ldots, \mu_{n1}, \ldots, \mu_{nm}]^T$, $b_l = [b_{l11}, \ldots, b_{l1n}, b_{l21}, \ldots, b_{l2n}, \ldots, b_{lv1}, \ldots, b_{lvn}]^T$, $b_r = [b_{r11}, \ldots, b_{r1n}, b_{r21}, \ldots, b_{r2n}, \ldots, b_{rv1}, \ldots, b_{rvn}]^T$, $c = [c_{11}, \ldots, c_{1n}, c_{21}, \ldots, c_{2n}, \ldots, c_{v1}, \ldots, c_{vn}]^T$, $\phi = [\phi_1, \phi_2, \ldots, \phi_v]^T$, $\theta = [\theta_1, \theta_2, \ldots, \theta_v]^T$, $\Phi = [\Phi_1, \Phi_2, \ldots, \Phi_v]^T$, $W_f = [w_{f1}, w_{f2}, \ldots, w_{fv}]^T$, $W_r =$

$[w_{r1}, w_{r2}, \ldots, w_{rv}]^T$, $W_h = [w_{h11}, \ldots, w_{h1v}, w_{h21}, \ldots, w_{h2v}, \ldots, w_{hz1}, \ldots, w_{hzv}]^T$.

Then, for the sake of presentation, the following definition is given.

Definition 1: For a variate ϖ, defines its ideal value and estimated value as ϖ^* and $\hat{\varpi}$, respectively. Consequently, the approximation error can be denoted as $\tilde{\varpi} = \varpi^* - \hat{\varpi}$.

Based on the abovementioned discussion, the approximation error between u_{FITSMC} and u_{HBFNN} can be given as

$$\begin{aligned}\tilde{u} &= u_{\text{FITSMC}} - u_{\text{HBFNN}} \\ &= W^{*T}Y^* - \hat{W}^T\hat{Y} + \varepsilon_0 \\ &= (\hat{W}^T + \tilde{W}^T)(\hat{Y} + \tilde{Y}) - \hat{W}^T\hat{Y} + \varepsilon_0 \\ &= \tilde{W}^T\hat{Y} + \hat{W}^T\tilde{Y} + \tilde{W}^T\tilde{Y} + \varepsilon_0 \\ &= \tilde{W}^T\hat{Y} + \hat{W}^T\tilde{Y} + \varepsilon_1 \end{aligned} \tag{31}$$

where ε_1 is the estimation error and $\varepsilon_1 = \tilde{W}^T\tilde{Y} + \varepsilon_0$.

Afterwards, taking the Taylor expansion of Y^* at $\hat{Y}$ yields

$$\begin{aligned}Y^* = \hat{Y} &+ \frac{\partial \hat{Y}}{\partial \sigma}\Big|_{\sigma=\hat{\sigma}}(\sigma^* - \hat{\sigma}) + \frac{\partial \hat{Y}}{\partial \mu}\Big|_{\mu=\hat{\mu}}(\mu^* - \hat{\mu}) \\ &+ \frac{\partial \hat{Y}}{\partial b_l}\Big|_{b_l=\hat{b}_l}({b_l}^* - \hat{b}_l) + \frac{\partial \hat{Y}}{\partial b_r}\Big|_{b_r=\hat{b}_r}({b_r}^* - \hat{b}_r) \\ &+ \frac{\partial \hat{Y}}{\partial c}\Big|_{c=\hat{c}}(c^* - \hat{c}) \\ &+ \frac{\partial \hat{Y}}{\partial \phi}\Big|_{\phi=\hat{\phi}}(\phi^* - \hat{\phi}) + \frac{\partial \hat{Y}}{\partial \theta}\Big|_{\theta=\hat{\theta}}(\theta^* - \hat{\theta}) \\ &+ \frac{\partial \hat{Y}}{\partial \Phi}\Big|_{\Phi=\hat{\Phi}}(\Phi^* - \hat{\Phi}) \\ &+ \frac{\partial \hat{Y}}{\partial W_f}\Big|_{W_f=\hat{W}_f}({W_f}^* - \hat{W}_f) \\ &+ \frac{\partial \hat{Y}}{\partial W_r}\Big|_{W_r=\hat{W}_r}({W_r}^* - \hat{W}_r) \\ &+ \frac{\partial \hat{Y}}{\partial W_h}\Big|_{W_h=\hat{W}_h}({W_h}^* - \hat{W}_h) + \delta \\ = \hat{Y} &+ \partial\hat{Y}_\sigma\tilde{\sigma} + \partial\hat{Y}_\mu\tilde{\mu} + \partial\hat{Y}_{b_l}\tilde{b}_l + \partial\hat{Y}_{b_r}\tilde{b}_r + \partial\hat{Y}_c\tilde{c} + \partial\hat{Y}_\phi\tilde{\phi} \\ &+ \partial\hat{Y}_\theta\tilde{\theta} + \partial\hat{Y}_\Phi\tilde{\Phi} + \partial\hat{Y}_{W_f}\tilde{W}_f + \partial\hat{Y}_{W_r}\tilde{W}_r \\ &+ \partial\hat{Y}_{W_h}\tilde{W}_h + \delta \end{aligned} \tag{32}$$

where δ is a high order expansion term, and further one can get

$$\begin{aligned}\tilde{Y} = &\partial\hat{Y}_\sigma\tilde{\sigma} + \partial\hat{Y}_\mu\tilde{\mu} + \partial\hat{Y}_{b_l}\tilde{b}_l + \partial\hat{Y}_{b_r}\tilde{b}_r + \partial\hat{Y}_c\tilde{c} + \partial\hat{Y}_\phi\tilde{\phi} \\ &+ \partial\hat{Y}_\theta\tilde{\theta} + \partial\hat{Y}_\Phi\tilde{\Phi} + \partial\hat{Y}_{W_f}\tilde{W}_f + \partial\hat{Y}_{W_r}\tilde{W}_r + \partial\hat{Y}_{W_h}\tilde{W}_h + \delta \end{aligned} \tag{33}$$

where

$$\partial\hat{Y}_\sigma = \begin{bmatrix} \frac{\partial\hat{y}_1}{\partial\sigma_{11}} \cdots \frac{\partial\hat{y}_1}{\partial\sigma_{1m}}, \ \cdots, \ \frac{\partial\hat{y}_1}{\partial\sigma_{n1}} \cdots \frac{\partial\hat{y}_1}{\partial\sigma_{nm}} \\ \vdots \ \cdots \ \vdots \quad \ddots \quad \vdots \ \cdots \ \vdots \\ \frac{\partial\hat{y}_z}{\partial\sigma_{11}} \cdots \frac{\partial\hat{y}_z}{\partial\sigma_{1m}}, \ \cdots, \ \frac{\partial\hat{y}_z}{\partial\sigma_{n1}} \cdots \frac{\partial\hat{y}_z}{\partial\sigma_{nm}} \end{bmatrix}$$

$$\partial\hat{Y}_\mu = \begin{bmatrix} \frac{\partial\hat{y}_1}{\partial\mu_{11}} \cdots \frac{\partial\hat{y}_1}{\partial\mu_{1m}}, \ \cdots, \ \frac{\partial\hat{y}_1}{\partial\mu_{n1}} \cdots \frac{\partial\hat{y}_1}{\partial\mu_{nm}} \\ \vdots \ \cdots \ \vdots \quad \ddots \quad \vdots \ \cdots \ \vdots \\ \frac{\partial\hat{y}_z}{\partial\mu_{11}} \cdots \frac{\partial\hat{y}_z}{\partial\mu_{1m}}, \ \cdots, \ \frac{\partial\hat{y}_z}{\partial\mu_{n1}} \cdots \frac{\partial\hat{y}_z}{\partial\mu_{nm}} \end{bmatrix}$$

$$\partial\hat{Y}_{b_l} = \begin{bmatrix} \frac{\partial\hat{y}_1}{\partial b_{l11}} \cdots \frac{\partial\hat{y}_1}{\partial b_{l1n}}, \ \cdots, \ \frac{\partial\hat{y}_1}{\partial b_{lv1}} \cdots \frac{\partial\hat{y}_1}{\partial b_{lvn}} \\ \vdots \ \cdots \ \vdots \quad \ddots \quad \vdots \ \cdots \ \vdots \\ \frac{\partial\hat{y}_z}{\partial b_{l11}} \cdots \frac{\partial\hat{y}_z}{\partial b_{l1n}}, \ \cdots, \ \frac{\partial\hat{y}_z}{\partial b_{lv1}} \cdots \frac{\partial\hat{y}_z}{\partial b_{lvn}} \end{bmatrix}$$

$$\partial\hat{Y}_{b_r} = \begin{bmatrix} \frac{\partial\hat{y}_1}{\partial b_{r11}} \cdots \frac{\partial\hat{y}_1}{\partial b_{r1n}}, \ \cdots, \ \frac{\partial\hat{y}_1}{\partial b_{rv1}} \cdots \frac{\partial\hat{y}_1}{\partial b_{rvn}} \\ \vdots \ \cdots \ \vdots \quad \ddots \quad \vdots \ \cdots \ \vdots \\ \frac{\partial\hat{y}_z}{\partial b_{r11}} \cdots \frac{\partial\hat{y}_z}{\partial b_{r1n}}, \ \cdots, \ \frac{\partial\hat{y}_z}{\partial b_{rv1}} \cdots \frac{\partial\hat{y}_z}{\partial b_{rvn}} \end{bmatrix}$$

$$\partial\hat{Y}_c = \begin{bmatrix} \frac{\partial\hat{y}_1}{\partial c_{11}} \cdots \frac{\partial\hat{y}_1}{\partial c_{1n}}, \ \cdots, \ \frac{\partial\hat{y}_1}{\partial c_{v1}} \cdots \frac{\partial\hat{y}_1}{\partial c_{vn}} \\ \vdots \ \cdots \ \vdots \quad \ddots \quad \vdots \ \cdots \ \vdots \\ \frac{\partial\hat{y}_z}{\partial c_{11}} \cdots \frac{\partial\hat{y}_z}{\partial c_{1n}}, \ \cdots, \ \frac{\partial\hat{y}_z}{\partial c_{v1}} \cdots \frac{\partial\hat{y}_z}{\partial c_{vn}} \end{bmatrix}$$

$$\partial\hat{Y}_\phi = \begin{bmatrix} \frac{\partial\hat{y}_1}{\partial\phi_1}, \frac{\partial\hat{y}_1}{\partial\phi_2}, \ldots, \frac{\partial\hat{y}_1}{\partial\phi_v} \\ \vdots \quad \ddots \quad \vdots \\ \frac{\partial\hat{y}_z}{\partial\phi_1}, \frac{\partial\hat{y}_z}{\partial\phi_2}, \ldots, \frac{\partial\hat{y}_z}{\partial\phi_v} \end{bmatrix}, \ \partial\hat{Y}_\theta = \begin{bmatrix} \frac{\partial\hat{y}_1}{\partial\theta_1}, \frac{\partial\hat{y}_1}{\partial\theta_2}, \ldots, \frac{\partial\hat{y}_1}{\partial\theta_v} \\ \vdots \quad \ddots \quad \vdots \\ \frac{\partial\hat{y}_z}{\partial\theta_1}, \frac{\partial\hat{y}_z}{\partial\theta_2}, \ldots, \frac{\partial\hat{y}_z}{\partial\theta_v} \end{bmatrix}$$

$$\partial\hat{Y}_\Phi = \begin{bmatrix} \frac{\partial\hat{y}_1}{\partial\Phi_1}, \frac{\partial\hat{y}_1}{\partial\Phi_2}, \ldots, \frac{\partial\hat{y}_1}{\partial\Phi_v} \\ \vdots \quad \ddots \quad \vdots \\ \frac{\partial\hat{y}_z}{\partial\Phi_1}, \frac{\partial\hat{y}_z}{\partial\Phi_2}, \ldots, \frac{\partial\hat{y}_z}{\partial\Phi_v} \end{bmatrix}, \ \partial\hat{Y}_{W_f} = \begin{bmatrix} \frac{\partial\hat{y}_1}{\partial w_{f1}}, \frac{\partial\hat{y}_1}{\partial w_{f2}}, \ldots, \frac{\partial\hat{y}_1}{\partial w_{fv}} \\ \vdots \quad \ddots \quad \vdots \\ \frac{\partial\hat{y}_z}{\partial w_{f1}}, \frac{\partial\hat{y}_z}{\partial w_{f2}}, \ldots, \frac{\partial\hat{y}_z}{\partial w_{fv}} \end{bmatrix}$$

$$\partial\hat{Y}_{W_r} = \begin{bmatrix} \frac{\partial\hat{y}_1}{\partial w_{r1}}, \frac{\partial\hat{y}_1}{\partial w_{r2}}, \ldots, \frac{\partial\hat{y}_1}{\partial w_{rv}} \\ \vdots \quad \ddots \quad \vdots \\ \frac{\partial\hat{y}_z}{\partial w_{r1}}, \frac{\partial\hat{y}_z}{\partial w_{r2}}, \ldots, \frac{\partial\hat{y}_z}{\partial w_{rv}} \end{bmatrix}$$

$$\partial\hat{Y}_{W_h} = \begin{bmatrix} \frac{\partial\hat{y}_1}{\partial w_{h11}} \cdots \frac{\partial\hat{y}_1}{\partial w_{h1v}}, \ \cdots, \ \frac{\partial\hat{y}_1}{\partial w_{hz1}} \cdots \frac{\partial\hat{y}_1}{\partial w_{hzv}} \\ \vdots \ \cdots \ \vdots \quad \ddots \quad \vdots \ \cdots \ \vdots \\ \frac{\partial\hat{y}_z}{\partial w_{h11}} \cdots \frac{\partial\hat{y}_z}{\partial w_{h1v}}, \ \cdots, \ \frac{\partial\hat{y}_z}{\partial w_{hz1}} \cdots \frac{\partial\hat{y}_z}{\partial w_{hzv}} \end{bmatrix}.$$

Then, substituting (33) into (31) yields

$$\begin{aligned}\tilde{u} &= u_{\text{FITSMC}} - u_{\text{HBFNN}} \\ &= \tilde{W}^T\hat{Y} + \hat{W}^T\tilde{Y} + \varepsilon_1 \\ &= \tilde{W}^T\hat{Y} + \hat{W}^T(\partial\hat{Y}_\sigma\tilde{\sigma} + \partial\hat{Y}_\mu\tilde{\mu} + \partial\hat{Y}_{b_l}\tilde{b}_l + \partial\hat{Y}_{b_r}\tilde{b}_r \\ &\quad + \partial\hat{Y}_c\tilde{c} + \partial\hat{Y}_\phi\tilde{\phi} \\ &\quad + \partial\hat{Y}_\theta\tilde{\theta} + \partial\hat{Y}_\Phi\tilde{\Phi} + \partial\hat{Y}_{W_f}\tilde{W}_f + \partial\hat{Y}_{W_r}\tilde{W}_r \\ &\quad + \partial\hat{Y}_{W_h}\tilde{W}_h + \delta) + \varepsilon_1 \\ &= \tilde{W}^T\hat{Y} + \hat{W}^T(\partial\hat{Y}_\sigma\tilde{\sigma} + \partial\hat{Y}_\mu\tilde{\mu} + \partial\hat{Y}_{b_l}\tilde{b}_l + \partial\hat{Y}_{b_r}\tilde{b}_r \\ &\quad + \partial\hat{Y}_c\tilde{c} + \partial\hat{Y}_\phi\tilde{\phi} \\ &\quad + \partial\hat{Y}_\theta\tilde{\theta} + \partial\hat{Y}_\Phi\tilde{\Phi} + \partial\hat{Y}_{W_f}\tilde{W}_f + \partial\hat{Y}_{W_r}\tilde{W}_r \end{aligned}$$

$$+\partial\hat{Y}_{W_h}\tilde{W}_h)+\delta_0 \tag{34}$$

where δ_0 is the total approximation error and its upper bound is supposed as ${\delta_d}^*$, which satisfies $|\delta_0|\le {\delta_d}^*$.

Then, the following adaptive compensation term is designed:

$$u_{\text{com}}=-\hat{\delta}_d\text{sgn}(s) \tag{35}$$

where $\hat{\delta}_d$ is the estimated value of ${\delta_d}^*$.

Thus, the final control law is designed as

$$\begin{aligned} u&=u_{\text{HBFNN}}+u_{\text{com}}\\ &=u_{\text{HBFNN}}-\hat{\delta}_d\text{sgn}(s). \end{aligned} \tag{36}$$

Subsequently substituting of (36) into (5) yields

$$\begin{aligned} \dot{s}&=f(i_c)+\psi(u_{\text{HBFNN}}+u_{\text{com}})+H-\ddot{i}_h+\alpha\dot{e}+\beta e^{p/q}\\ &=f(i_c)+\psi(u_{\text{FITSMC}}-\tilde{u}+u_{\text{com}})+H-\ddot{i}_h+\alpha\dot{e}+\beta e^{p/q}\\ &=H-\eta\text{sgn}(s)-\psi\hat{\delta}_d\text{sgn}(s)-\psi\tilde{u}. \end{aligned} \tag{37}$$

Then, setting the adaptive laws as

$$\begin{aligned} \dot{\hat{W}}^T&=-\dot{\tilde{W}}^T=-\eta_1 s\hat{Y}^T,\quad \dot{\hat{\sigma}}^T=-\dot{\tilde{\sigma}}^T=-\eta_2 s\hat{W}^T\partial\hat{Y}_\sigma\\ \dot{\hat{\mu}}^T&=-\dot{\tilde{\mu}}^T=-\eta_3 s\hat{W}^T\partial\hat{Y}_\mu,\quad \dot{\hat{b}}_l^{\,T}=-\dot{\tilde{b}}_l^{\,T}=-\eta_4 s\hat{W}^T\partial\hat{Y}_{b_l}\\ \dot{\hat{b}}_r^{\,T}&=-\dot{\tilde{b}}_r^{\,T}=-\eta_5 s\hat{W}^T\partial\hat{Y}_{b_r},\quad \dot{\hat{c}}^T=-\dot{\tilde{c}}^T=-\eta_6 s\hat{W}^T\partial\hat{Y}_c\\ \dot{\hat{\phi}}^T&=-\dot{\tilde{\phi}}^T=-\eta_7 s\hat{W}^T\partial\hat{Y}_\phi,\quad \dot{\hat{\theta}}^T=-\dot{\tilde{\theta}}^T=-\eta_8 s\hat{W}^T\partial\hat{Y}_\theta\\ \dot{\hat{\Phi}}^T&=-\dot{\tilde{\Phi}}^T=-\eta_9 s\hat{W}^T\partial\hat{Y}_\Phi,\quad \dot{\hat{W}}_f^{\,T}=-\dot{\tilde{W}}_f^{\,T}\\ &=-\eta_{10}s\hat{W}^T\partial\hat{Y}_{W_f}\\ \dot{\hat{W}}_r^{\,T}&=-\dot{\tilde{W}}_r^{\,T}=-\eta_{11}s\hat{W}^T\partial\hat{Y}_{W_r},\quad \dot{\hat{W}}_h^{\,T}\\ &=-\dot{\tilde{W}}_h^{\,T}=-\eta_{12}s\hat{W}^T\partial\hat{Y}_{W_h}\\ \dot{\hat{\delta}}_d&=-\dot{\tilde{\delta}}_d=\eta_{13}|s| \end{aligned} \tag{38}$$

where η_1–η_{13} are positive real numbers.

Theorem 1: For the perturbed APF model in (1), the fast integral terminal sliding surface is designed as (4), the final controller utilizing HBFNN is designed as (36), and the adaptive laws are set as (38), consequently, all signals included in (39) are bounded.

Eventually, in accordance with the abovementioned discussion, the following proof is given.

Proof: Choose the following Lyapunov function:

$$\begin{aligned} V_r=&\frac{1}{2}\psi^{-1}s^2+\frac{1}{2\eta_1}\text{tr}(\tilde{W}^T\tilde{W})+\frac{1}{2\eta_2}\text{tr}(\tilde{\sigma}^T\tilde{\sigma})\\ &+\frac{1}{2\eta_3}\text{tr}(\tilde{\mu}^T\tilde{\mu})+\frac{1}{2\eta_4}\text{tr}(\tilde{b}_l^T\tilde{b}_l)+\frac{1}{2\eta_5}\text{tr}(\tilde{b}_r^T\tilde{b}_r)\\ &+\frac{1}{2\eta_6}\text{tr}(\tilde{c}^T\tilde{c})+\frac{1}{2\eta_7}\text{tr}(\tilde{\phi}^T\tilde{\phi})+\frac{1}{2\eta_8}\text{tr}(\tilde{\theta}^T\tilde{\theta})\\ &+\frac{1}{2\eta_9}\text{tr}(\tilde{\Phi}^T\tilde{\Phi})+\frac{1}{2\eta_{10}}\text{tr}(\tilde{W}_f^T\tilde{W}_f)+\frac{1}{2\eta_{11}}\text{tr}(\tilde{W}_r^T\tilde{W}_r)\\ &+\frac{1}{2\eta_{12}}\text{tr}(\tilde{W}_h^T\tilde{W}_h)+\frac{1}{2\eta_{13}}\tilde{\delta}_d^2. \end{aligned} \tag{39}$$

Taking the derivative of it yields

$$\begin{aligned} \dot{V}_r=&\psi^{-1}s\dot{s}+\frac{1}{\eta_1}\text{tr}(\dot{\tilde{W}}^T\tilde{W})+\frac{1}{\eta_2}\text{tr}(\dot{\tilde{\sigma}}^T\tilde{\sigma})+\frac{1}{\eta_3}\text{tr}(\dot{\tilde{\mu}}^T\tilde{\mu})\\ &+\frac{1}{\eta_4}\text{tr}(\dot{\tilde{b}}_l^{\,T}\tilde{b}_l)+\frac{1}{\eta_5}\text{tr}(\dot{\tilde{b}}_r^{\,T}\tilde{b}_r)+\frac{1}{\eta_6}\text{tr}(\dot{\tilde{c}}^T\tilde{c})+\frac{1}{\eta_7}\text{tr}(\dot{\tilde{\phi}}^T\tilde{\phi})\\ &+\frac{1}{\eta_8}\text{tr}(\dot{\tilde{\theta}}^T\tilde{\theta})+\frac{1}{\eta_9}\text{tr}(\dot{\tilde{\Phi}}^T\tilde{\Phi})+\frac{1}{\eta_{10}}\text{tr}(\dot{\tilde{W}}_f^{\,T}\tilde{W}_f)\\ &+\frac{1}{\eta_{11}}\text{tr}(\dot{\tilde{W}}_r^{\,T}\tilde{W}_r)+\frac{1}{\eta_{12}}\text{tr}(\dot{\tilde{W}}_h^{\,T}\tilde{W}_h)+\frac{1}{\eta_{13}}\dot{\tilde{\delta}}_d\tilde{\delta}_d. \end{aligned} \tag{40}$$

Denote

$$\begin{aligned} &\frac{1}{\eta_1}\text{tr}(\dot{\tilde{W}}^T\tilde{W})+\frac{1}{\eta_2}\text{tr}(\dot{\tilde{\sigma}}^T\tilde{\sigma})+\frac{1}{\eta_3}\text{tr}(\dot{\tilde{\mu}}^T\tilde{\mu})+\frac{1}{\eta_4}\text{tr}(\dot{\tilde{b}}_l^{\,T}\tilde{b}_l)\\ &+\frac{1}{\eta_5}\text{tr}(\dot{\tilde{b}}_r^{\,T}\tilde{b}_r)+\frac{1}{\eta_6}\text{tr}(\dot{\tilde{c}}^T\tilde{c})+\frac{1}{\eta_7}\text{tr}(\dot{\tilde{\phi}}^T\tilde{\phi})+\frac{1}{\eta_8}\text{tr}(\dot{\tilde{\theta}}^T\tilde{\theta})\\ &+\frac{1}{\eta_9}\text{tr}(\dot{\tilde{\Phi}}^T\tilde{\Phi})+\frac{1}{\eta_{10}}\text{tr}(\dot{\tilde{W}}_f^{\,T}\tilde{W}_f)+\frac{1}{\eta_{11}}\text{tr}(\dot{\tilde{W}}_r^{\,T}\tilde{W}_r)\\ &+\frac{1}{\eta_{12}}\text{tr}(\dot{\tilde{W}}_h^{\,T}\tilde{W}_h)+\frac{1}{\eta_{13}}\dot{\tilde{\delta}}_d\tilde{\delta}_d \end{aligned}$$

as F to simplified expression. Combining (40) with (37) and (34) yields

$$\begin{aligned} \dot{V}_r=&\psi^{-1}s\cdot\left[H-\eta\,\text{sgn}(s)-\psi\hat{\delta}_d\,\text{sgn}(s)-\psi\tilde{u}\right]+F\\ =&\psi^{-1}s\cdot(H-\eta\,\text{sgn}(s))-\hat{\delta}_d|s|-s[\tilde{W}^T\hat{Y}+\hat{W}^T(\partial\hat{Y}_\sigma\tilde{\sigma}\\ &+\partial\hat{Y}_\mu\tilde{\mu}+\partial\hat{Y}_{b_l}\tilde{b}_l+\partial\hat{Y}_{b_r}\tilde{b}_r+\partial\hat{Y}_c\tilde{c}+\partial\hat{Y}_\phi\tilde{\phi}\\ &+\partial\hat{Y}_\theta\tilde{\theta}+\partial\hat{Y}_\Phi\tilde{\Phi}\\ &+\partial\hat{Y}_{W_f}\tilde{W}_f+\partial\hat{Y}_{W_r}\tilde{W}_r+\partial\hat{Y}_{W_h}\tilde{W}_h)+\delta_0]+F. \end{aligned} \tag{41}$$

Then, substituting the adaptive laws (38) into (41), one can get

$$\begin{aligned} \dot{V}_r&=\psi^{-1}s\cdot(H-\eta\,\text{sgn}(s))-\hat{\delta}_d|s|-\delta_0 s+\frac{1}{\eta_{13}}\dot{\tilde{\delta}}_d\tilde{\delta}_d\\ &=\psi^{-1}s\cdot(H-\eta\,\text{sgn}(s))-\hat{\delta}_d|s|-\delta_0 s-\tilde{\delta}_d|s|\\ &=\psi^{-1}s\cdot(H-\eta\,\text{sgn}(s))-(\hat{\delta}_d+\tilde{\delta}_d)|s|-\delta_0 s\\ &=\psi^{-1}s\cdot(H-\eta\,\text{sgn}(s))-\delta_d^*|s|-\delta_0 s. \end{aligned} \tag{42}$$

By using (12), the following expression can be obtained:

$$\begin{aligned} \dot{V}_r\le&\psi^{-1}\cdot(-\varepsilon|s|)-\delta_d^*|s|-\delta_0 s=-\psi^{-1}\varepsilon|s|\\ &-(\delta_d^*|s|+\delta_0 s). \end{aligned} \tag{43}$$

Since $|\delta_0|\le\delta_d^*$, so $\delta_d^*|s|+\delta_0 s\ge 0$. Hence, it can ultimately be obtained that

$$\begin{aligned} \dot{V}_r&\le-\psi^{-1}\varepsilon|s|\\ &\le 0. \end{aligned} \tag{44}$$

In accordance with Lyapunov stability criteria and Lemma 1, since V_r is positive definite and $\dot{V}_r$ is seminegative definite, the

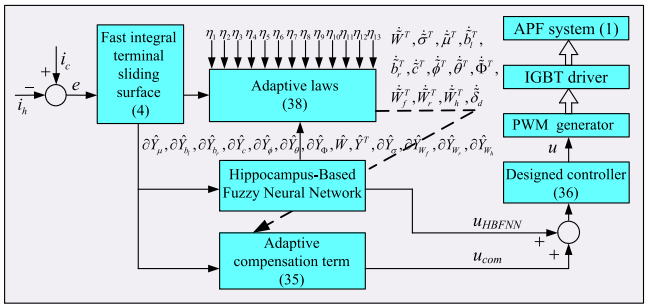

Fig. 5. Block diagram of HBFNN for APF.

TABLE I
SYSTEM PARAMETERS

Items	Specifications
Supply voltage and frequency	$U_s = 24$ V, $f = 50$ Hz
Nonlinear load 1	$R_1 = 5\ \Omega, R_2 = 15\ \Omega, C_{L1} = 1$ mf
Nonlinear load 2	$R_3 = 15\ \Omega, R_4 = 15\ \Omega, C_{L2} = 1$ mf
Main circuit	$L = 10$ mH, $R = 0.1\ \Omega, C = 2200\ \mu$F, $U_{dc}^{*} = 50$ V
Switching frequency	$f_{sw} = 20$ kHz

closed-loop stability can be guaranteed and all signals in (39) are bounded. So far, the proof has been completed. And the block diagram of the proposed control strategy for APF is depicted in Fig. 5.

Remark 3: The hybrid control method in this article combines FITSMC with HBFNN. The proposed FITSMC ensures that the tracking error of the system can converge to zero in a finite time. Then, in order to enhance FITSMC, we construct a novel HBFNN to learn it.

Remark 4: In this article, the closed-loop stability is proved strictly by Lyapunov stability theorem. In addition, the adaptive laws of the parameters are derived such that the parameters in the HBFNN can be automatically updated online, which can save the time of selecting the optimal initial values and enhance the self-adaptive ability of HBFNN.

V. Simulation and Experiment Validation

Fig. 5 depicts the overall control block diagram of HBFNN for APF. Based on this, in this section, a series of simulation and hardware experiments are carried out to validate the effectiveness and practicability of the designed controller, which are operated on MATLAB/Simulink and dSPACE 1104 experiment platform respectively. The APF begins to work when $t = 0.04$s.

A. Simulation

The network structure of HBFNN is designed as $m = 2, n = 3, \nu = 4, z = 3$, and all initial parameters are selected as follows: W=$[1,1,1]^T$,W_h=$[1,1,1,1,1,1,1,1,1,1,1,1,1]^T$, W_r=$[1,1,1,1,1,1,1,1,1,1,1,1,1]^T$,$W_f$=$[1,1,1,1,1,1,1,1,1,1,1,1]^T$,$\sigma = [3,3,3,3,3,3]^T$, $\mu = [-3,-2,-1,1,2,3]^T$, b_l=$[2,2,2,2,2,2,2,2,2,2,2,2]^T$,$b_r$=$[3,3,3,3,3,3,3,3,3,3,3,3]^T$, c=$[-5,-4,-3,-2,-1,0,1,2,3,4,5,6]^T$, ϕ=$[1,1,1,1]^T$, θ=$[1,1,1,1]^T$, $\Phi = [-2,-1,1,2]^T$, $\hat{\delta}_d = 15$, α=10, β=20, $p = 3$, $q = 5$, $D_t = 0.1$, η=100, $\eta_1 = 0.5$, $\eta_2 = 0.2$, $\eta_3 = 0.4$,$\eta_4 = 0.1$, $\eta_5 = 0.6$, $\eta_6 = 0.4$, $\eta_7 = 0.7$, $\eta_8 = 0.3$, $\eta_9 = 0.2$, $\eta_{10} = 0.5$, $\eta_{11} = 0.4$, $\eta_{12} = 0.8$, $\eta_{13} = 400$. In addition, the system parameters are listed in Table I.

Remark 5: The proposed control scheme has many parameters and the selection of these parameters can influence the control effect. In this article, we utilize the empirical rule and trial-and-error method to select the specific values of parameters [48], [49], [50].

$\alpha, \beta, p/q$ are the parameters of the sliding surface. According to empirical rules, appropriately increasing these parameters will accelerate the response speed of the system. However, when these parameters are too large, the tracking error of the system may fail to converge. Therefore, we choose $\alpha = 10$, $\beta = 20$, $p = 3$, $q = 5$.

D_t is the predesigned threshold value in the DG layer. If D_t is too large, many nodes will be deleted, which will reduce the computing burden of the network, but also make the approximation ability of the network decrease. If the D_t is too small, the nodes in the network are not easily deleted, and the computing burden of the network is relatively large. Therefore, by balancing the control performance and computation amount, we choose $D_t = 0.1$.

According to the Lyapunov stability theorem, η_1–η_{13} should all be more than zero. By empirical rule, too large η_1–η_{13} may result in divergence control responses. However, too small η_1–η_{13} may make the network parameters unable to change swiftly to deal with sudden interference. Therefore, we choose $\eta_1 = 0.5$, $\eta_2 = 0.2$, $\eta_3 = 0.4$, $\eta_4 = 0.1$, $\eta_5 = 0.6$, $\eta_6 = 0.4$, $\eta_7 = 0.7$, $\eta_8 = 0.3$, $\eta_9 = 0.2$, $\eta_{10} = 0.5$, $\eta_{11} = 0.4$, $\eta_{12} = 0.8$, $\eta_{13} = 400$.

In Fig. 5, the reference compensation current i_h is equal in magnitude and opposite in direction to the harmonic current. The designed controller (36) is used to drive IGBT unit to generate actual compensation current i_c to track the reference compensation current i_h to offset harmonic current, thereby achieving the effect of improving the power quality of the power grid.

1) Steady-State Performance: Fig. 6(a) and (b) shows the steady-state simulation waveform, where U_s, i_L, i_s,i_h, and $i_c$correspond to source voltage, load current, source current, reference compensation current, and compensation current. Generally, total harmonic distortion (THD) is used as an indicator to measure the severity of waveform distortion caused by harmonics. Before using the proposed APF for compensation, i_s is exactly the same as i_L and the THD of i_s is equal to that of i_L. From Fig. 6(c), before the proposed APF is used for compensation, the THD of i_s and i_L are both as high as 40.3%. After compensating with the proposed APF, the THD of i_L is still 40.3% and the THD of i_s is reduced to 1.24%. Consequently, from these observations, it can be concluded that the developed HBFNN controller has the superior control performance in harmonic elimination under steady-state

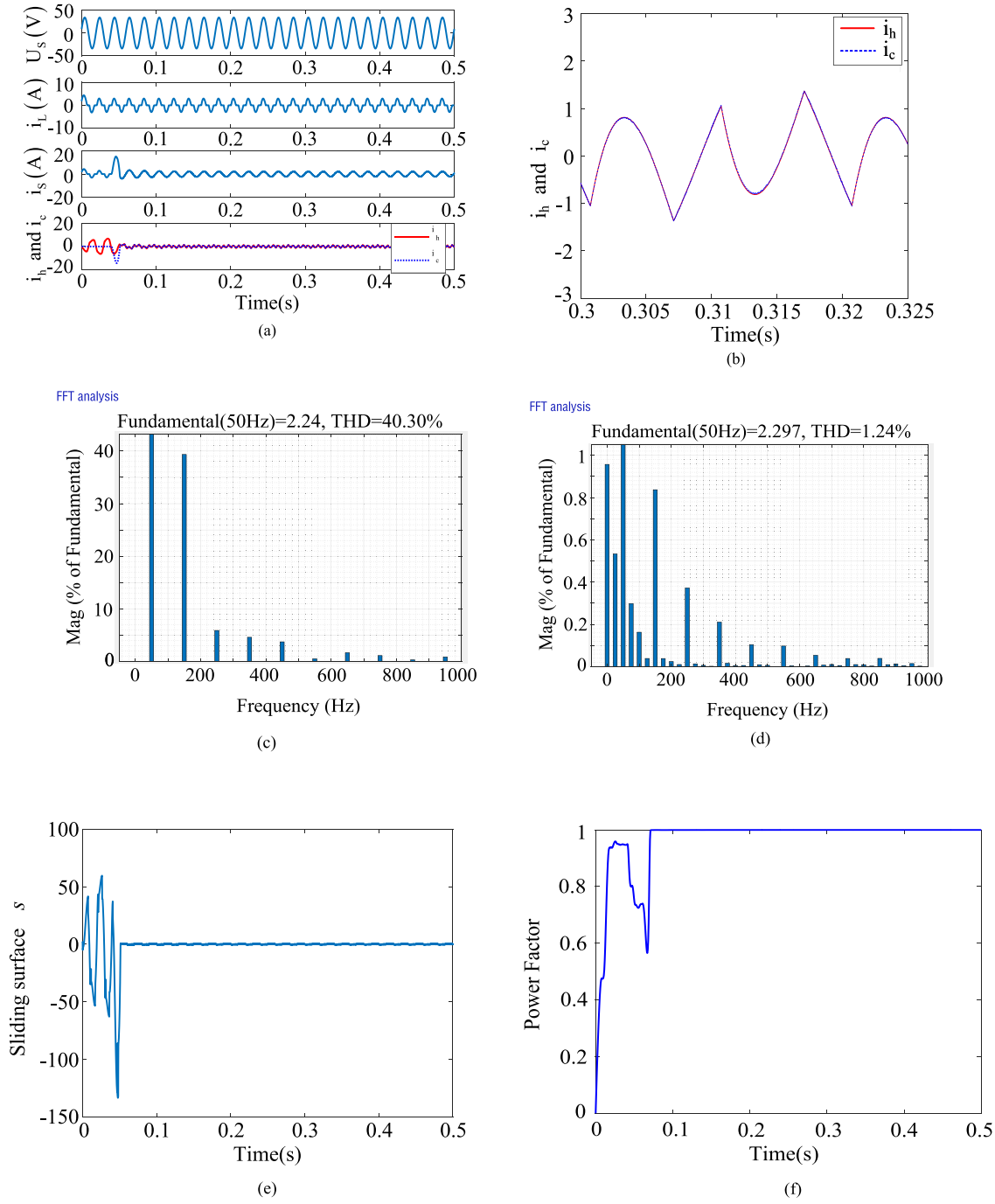

Fig. 6. Steady-state simulation results using HBFNN controller. (a) Simulation waveform. (b) Reference compensation current and compensation current. (c) THD of i_L. (d) THD of i_s. (e) Variation trend of s. (f) Power factor.

conditions. In Fig. 6(e), the sliding surface s quickly reaches a convergence state and then remains stable. From Fig. 6(f), after adopting the proposed APF, the power factor curve converges rapidly and then remains stable at 1, which indicates that the proposed controller has a good reactive power compensation effect.

Remark 6: The aim of APF is to reshape the source current to be a sine wave in phase with the sinusoidal source voltage [51]. To achieve this purpose, the reference compensation current can be expressed as

$$i_h = i_L - \gamma E_s \sin(\omega_s t) \tag{45}$$

where γ is a suitable value that sets the source current amplitude and E_s and ω_s are the peak value and angular frequency of the source voltage, respectively.

Remark 7: As mentioned in Remark 6, the reference compensation current i_h can be expressed as (45). Using the proposed controller, the tracking error between i_c and i_h will be converge

to zero in finite time. In this case, one can obtain $i_c = i_h$, leading to the following expression:

$$i_c = i_L - \gamma E_s \sin(\omega_s t). \tag{46}$$

In addition, one can get (47) from Fig. 1

$$i_s + i_c = i_L. \tag{47}$$

Substituting (46) into (47), one can conclude

$$i_s = \gamma E_s \sin(\omega_s t). \tag{48}$$

It is obvious that the source current is made proportional to the sinusoidal source voltage, thus maintaining satisfactory power factor correction operation [52], [53].

2) Load Mutation: To further reveal the dynamic characteristics of the proposed control scheme, simulations are carried out under dynamic load. Fig. 7(a) and (b) represents the simulation waveform of sudden increase and sudden decrease of load at 0.25 s, respectively. Apparently, it can be found that no matter what changes in the load, i_c can still track the i_h accurately and i_s still maintains the sine wave state. Meanwhile, from Fig. 7(c) and (d), it can be noted that THD of i_s is 0.98% when the load increases and 1.29% when the load decreases, which indicates that the developed HBFNN controller still has remarkable performance in harmonic suppression under dynamic load. In Fig. 7(e) and (f), load mutation has almost no impact on the power factor. Thus, in accordance with the abovementioned discussion, a natural conclusion can be drawn that proposed control scheme not only has the brilliant control performance but also possesses strong robustness. In Fig. 8(a) and (b), the sliding surface s can rapidly converge and maintain stability when the load changes abruptly.

3) Voltage Disturbance: In practical applications, since the environment is constantly changing, there exist some unexpected events that will cause voltage fluctuations. Hence, in order to verify the insensitivity of HBFNN controller against perturbation, the simulations are conducted under voltage decrease and voltage increase. Fig. 9(a) and (b) exhibits the simulation waveform when the voltage suddenly decreases and increases, respectively. It can be observed that even if the voltage drops, i_s still presents a sine wave, and i_c can still accurately track the reference compensation current i_h. In Fig. 9(c) and (d), the THD of i_s under voltage decrease is 1.47% and the THD of i_s under voltage increase is 1.35%. In Fig. 9(e) and (f), faced with sudden voltage disturbances, the power factor curve can recover to 1 in a very short time, which indicates that the proposed control scheme can perform reactive power compensation under unstable voltage environment. Therefore, based on the abovementioned results, one can be concluded that no matter whether the voltage fluctuation occurs, the designed HBFNN controller has strong anti-interference and can still show excellent control performance. In Fig. 10(a) and (b), when the voltage suddenly changes, the sliding surface s can be adjusted quickly and maintain stability.

4) Comparative Analysis: In order to demonstrate the "fast" feature of the proposed FITSMC, we have selected the adaptive fast nonsingular terminal sliding-mode controller (AFNTSMC) [54] and the global sliding-mode controller (GSMC) [55] as comparison objects. Fig. 11 shows the comparison diagram of the tracking error curves of different SMC. One can find that the tracking error curve corresponding to the proposed FITSMC is the first to reach the convergence state, showing that FITSMC has faster convergence speed and better tracking performance. In Table II, the THD of the FITSMC is the smallest among these three sliding surfaces, indicating that FITSMC has higher control accuracy.

TABLE II
THD OF DIFFERENT CONTROLLERS

Controller	FITSMC	AFNTSMC	GSMC
THD (%)	4.85	5.69	6.13

TABLE III
THD, RMSE, AND ET OF DIFFERENT CONTROLLERS

Controller	THD (%)	RMSE	ET (s)
FITSMC	4.85	3.5869	36
FNN	3.78	2.0456	47
RNN	2.70	1.9289	52
T2FNN	2.63	1.7138	75
HBFNN	1.24	1.2332	91

To further highlight the superiority of the proposed HBFNN controller, in this part, the Type-2 fuzzy neural network (T2FNN) controller [56], RNN controller [30], and FNN controller [41] and FITSMC are adopted as its comparison objects for comparative simulation. Fig. 12 presents the comparison of tracking error trajectories of these five different control schemes. It is evident from Fig. 12 that the proposed HBFNN control scheme has superior control characteristics, such as faster convergence speed and higher control precision. Subsequently, in order to show the comparison of control effect about these five controllers more intuitively, their respective THD, root mean squared error (RMSE), and execution time (ET) are listed in Table III. The RMSE stands for root mean square error, which is used as the error reference index here, and its mathematical expression can be denoted as

$$RMSE = \sqrt{\frac{1}{n}\sum_{i=1}^{n} e^2(i)}. \tag{49}$$

According to Table III, the ET of the proposed scheme is relatively longer because the proposed HBFNN has many weights and parameters. However, recently, with the unprecedented development of very large-scale integration technology, the computing power of microprocessors has been remarkably improved. Under this circumstance, by using the high-performance microprocessor, we can realize the control algorithm with high computational complexity. Therefore, utilizing current advanced dSPACE to realize the designed control scheme is not difficult. Besides, the experimental part of this article (e.g., Figs. 15–17) also proves that the proposed control method can show good harmonic suppression effect and dynamic performance through dSPACE. Moreover, in Table III, among these five control schemes, the THD and RMSE of the developed

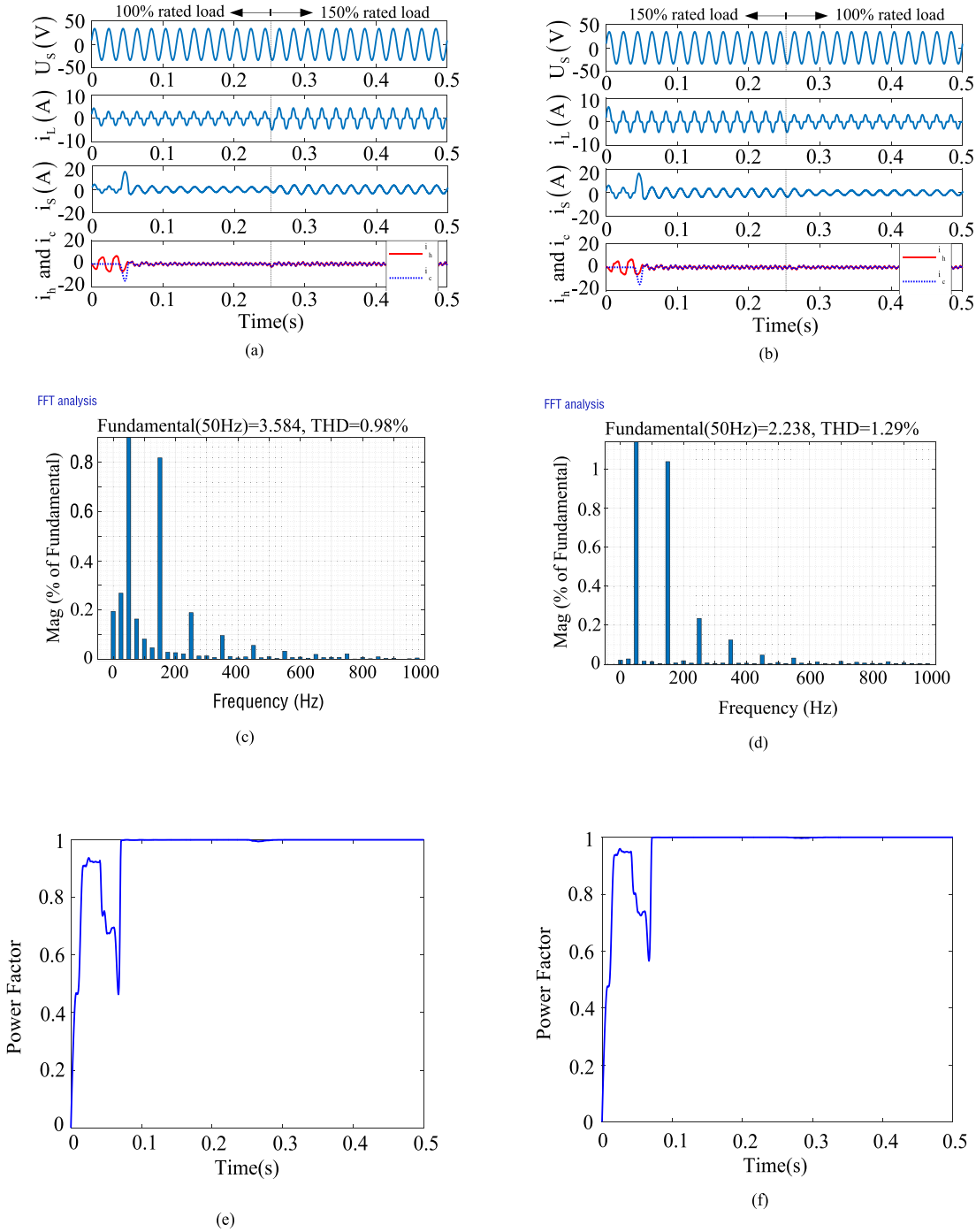

Fig. 7. Simulation results under dynamic load. (a) Load increase at 0.25 s. (b) Load decrease at 0.25 s. (c) THD under load increase. (d) THD under load decrease. (e) Power factor under load increase. (f) Power factor under load decrease.

HBFNN controller are smaller, indicating that the designed HBFNN controller has a better control performance and dynamic characteristics compared with other four control schemes.

B. Experiment

The abovementioned simulation results only demonstrate that the proposed control method reveals an excellent performance in the ideal simulation environment. To further reveal the feasibility and effectiveness of the developed control scheme in practical applications, the following series of hardware experiments are carried out by means of the experimental platform as shown in Fig. 13, which is formed of APF, dSPACE 1104, oscilloscope, dc source, and programmable ac voltage. The values of system parameters in the experimental section are exactly the same as the values of system parameters in the simulation section.

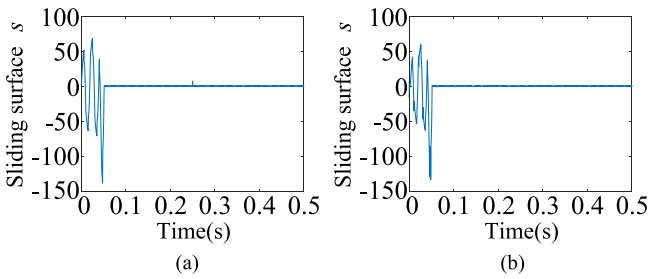

Fig. 8. Dynamic simulation results. (a) Variation trend of s under load increase. (b) Variation trend of s under load decrease.

Therefore, the values of system parameters in the experimental section are also shown in Table I.

The specific functions of the experimental equipment on the APF experimental platform are as follows. As the control core of the whole circuit, dSPACE 1104 is used to realize the calculation task of the designed control algorithm. DC source is used to supply power to dc devices in the APF experimental platform, such as hall sensors, IGBT drive unit. The oscilloscope is used to display waveform and calculate the harmonic content of current signal in real time. Programmable ac power is mainly used to provide simulated power grid environment.

The parameter value of dc-link capacitor C can be selected according to the following empirical formula [57], [58]:

$$C_{\min} = \frac{S_c T}{\lambda\left(1+\lambda\right) U_{\mathrm{dc}}^2} \tag{50}$$

where T represents the period of dc voltage control and $T = 1/2000$ s, λdenotes dc voltage fluctuation rate and $\lambda = 0.1$, $U_{\mathrm{dc}} = 50$ V, S_c is the capacity of APF and $S_c = 41$ W. So we can obtain $C_{\min} = 74$ μF. However, it is difficult to obtain a power capacitor with such a small capacitance in practical situation. Therefore, we ultimately choose EPCOS company's electrolytic capacitor C whose model is B43310-A5228-M and $C = 2200$ μF.

The parameter value of ac reactor L can be selected according to the following empirical formula [57], [58]:

$$L = \frac{4U_{\mathrm{dc}}}{9\Theta} \tag{51}$$

where $\Theta = k_1 \frac{i_{h\max}}{T_s}$, T_s denotes the period of current control and $T_s = 1/20\,000$ s, $i_{h\max}$ represents the maximum value of reference compensation current, $k_1 = 0.3$, $U_{\mathrm{dc}} = 50$ V. So we can obtain $L = 1.5$ mH. To improve the compensation performance, we finally choose $L = 10$ mH.

The experimental steps of the proposed control algorithm are as follows.

1) The APF simulation platform is built in MATLAB/Simulink and the proposed controller is used to control APF. The sampling time is 50 μs.
2) Replace the input and output of APF system in MATLAB/Simulink with the modules, which are matched with dSPACE 1104, and the MATLAB codes will be converted into C codes automatically, which is convenient to be run in dSPACE 1104.
3) Compile obtained C codes with control desk software and download the compiled content to dSPACE 1104.
4) Implement the final C codes (i.e., the proposed HBFNN control scheme) with dSPAPE 1104 online. The sampling time is 50 μs.

Fig. 14 depicts the schematic of the HBFNN in MATLAB/Simulink. The HBFNN is run in the form of code in MATLAB/Simulink as shown in Fig. 14.

1) Steady State: Fig. 15(a) depicts the experimental waveform of the proposed control scheme under steady state. Apparently, it can be seen that i_s presents a sinusoidal state, indicating that the harmonic current is suppressed. Besides, Fig. 15(b) shows the harmonic spectrum analysis of source current using HBFNN, T2FNN, RNN, FNN, and FITSMC. All the abovementioned results suggest that the developed HBFNN controller has superior performance under steady state.

2) Dynamic Load: In order to further reveal the characteristics of the proposed HBFNN controller, a series of experiments are carried out under the condition of dynamic load. Fig. 16(a) and (b) shows the experimental waveform using the proposed HBFNN controller when loads decrease and loads increase, respectively. In Fig. 16(a) and (b), when the load increases or decreases abruptly, the proposed controller can quickly generate the correct compensation current, the source current can always maintain the sinusoidal shape, and the curve of source current is very smooth. Correspondingly, Fig. 16(c) and (d) presents three-dimensional histograms of the source current harmonic spectrum under the action of these controllers when loads decrease and loads increase, respectively. From Fig. 16(c) and (d), among these five comparison methods, the harmonic content using HBFNN is at a low level and the THD of source current using HBFNN is the lowest, indicating that the proposed HBFNN controller has strong robustness and better harmonic suppression capability.

3) Voltage Variation: Fig. 17(a) and (b) shows the experimental waveform using the proposed HBFNN controller when voltage increases and decreases, respectively. As can be seen from Fig. 17(a) and (b), when the voltage suddenly increases or decreases, the source current can quickly transform from one kind of sinusoidal shape to another kind of sinusoidal shape. Likewise, Fig. 17(c) and (d) also shows the three-dimensional histograms of the source current harmonic spectrum under the action of five controllers when voltage increases and decreases, respectively. In Fig. 17(c) and (d), among these five comparison methods, the proposed method has stronger harmonic suppression ability regardless of voltage suddenly increases or decreases. Meanwhile, it also reflects that the designed HBFNN controller can still have superior control effect and excellent anti-interference performance in the practical operation environment under voltage mutations.

4) Parameter Variation of APF: In the parametric perturbation experiment, the inductance L varies from 6 to 10 mH, and the dc-link capacitor C varies from 1000 to 3300 μF. Table IV summarizes the THD of i_s under different parameters. In Table IV, it is observed that the THD of i_s changes little and is always lower than the normal range (5%), which indicates the superior robustness of the proposed method in case of parameter variations.

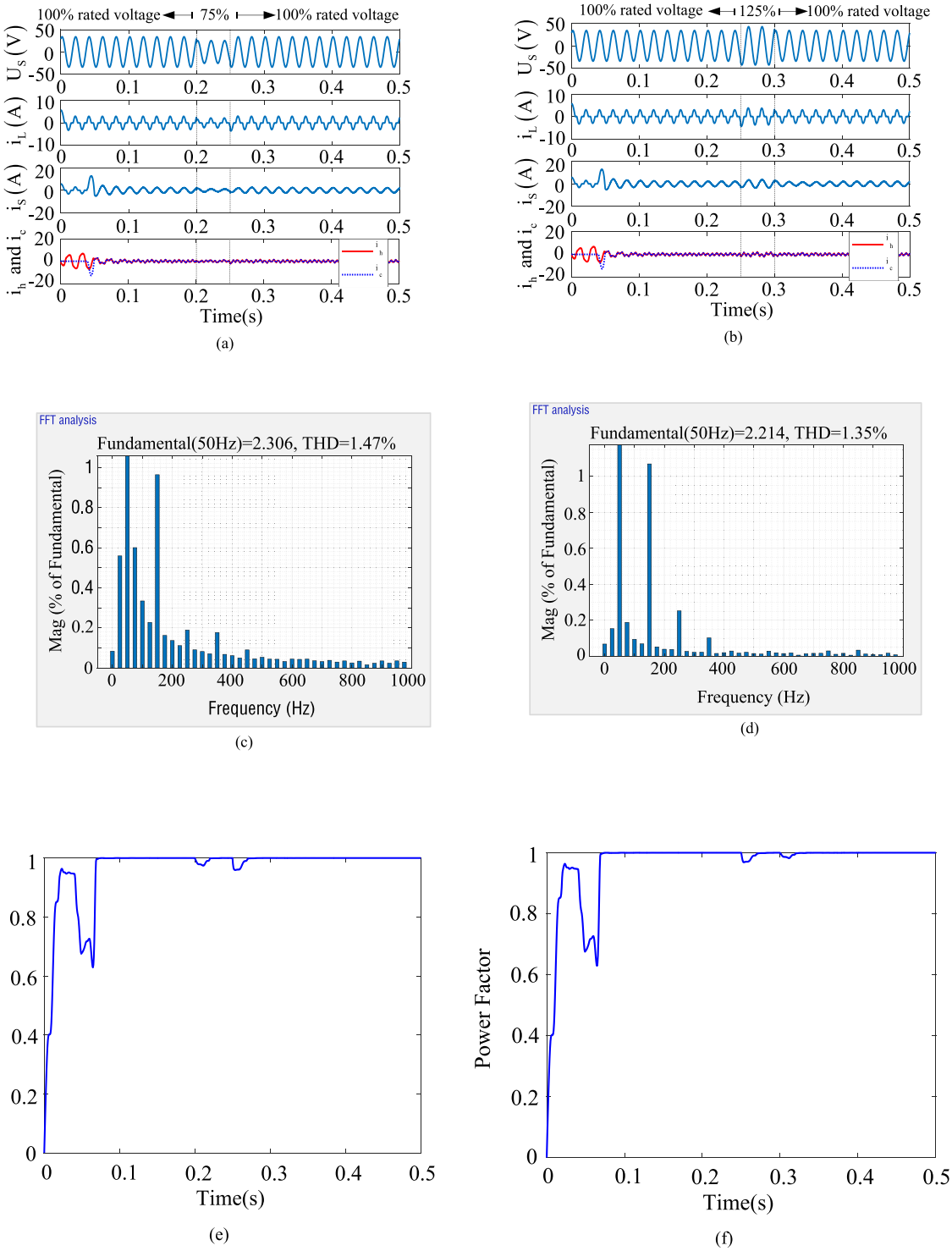

Fig. 9. Simulation results with voltage disturbance. (a) Voltage decrease. (b) Voltage increase. (c) THD under voltage decrease. (d) THD under voltage increase. (e) Power factor under voltage decrease. (f) Power factor under voltage increase.

5) Comparative Analysis: Furthermore, to more intuitively and clearly reveal the superiority of the proposed control scheme, the THD of these five control schemes in various cases are listed in Table V. By observing the THD of source current corresponding to the HBFNN controller in Table V alone, it can be found that the THD of source current corresponding to the HBFNN controller changes little under different experiments, indicating that the harmonic suppression ability of the HBFNN controller is relatively stable. Comparing the THD values of these five controllers in Table V, it can be found that no matter which experiment is conducted, the THD value corresponding to the HBFNN controller is lower than that using other four controllers,

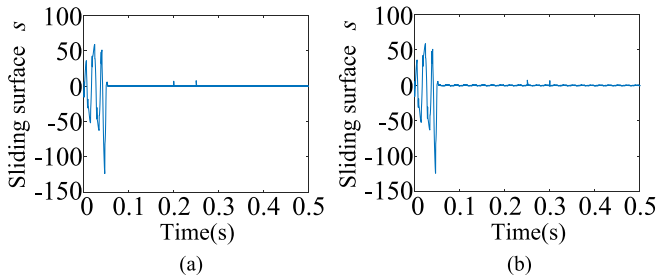

Fig. 10. Dynamic simulation results. (a) Variation trend of s under voltage decrease. (b) Variation trend of s under voltage increase.

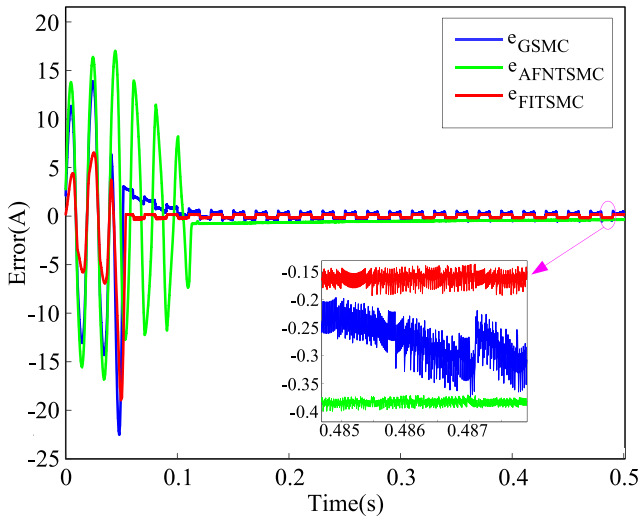

Fig. 11. Tracking error curves of different SMC.

TABLE IV
EFFECT OF PARAMETER CHANGES

Inductance (mH)	DC-link capacitor (μF)	THD (%)
10	2200	2.96
10	1000	3.47
10	3300	3.25
6	2200	4.72
8	2200	3.19

suggesting that adopting the HBFNN controller results in lower harmonic content and higher power quality in the power grid.

Remark 8: The conventional fuzzy-based controller has robust feature, but the conventional fuzzy-based controller can only make the tracking error asymptotically converge to zero. Compared with the conventional fuzzy-based controller [59], [60], the proposed FITSMC not only has excellent robustness, but also can ensure that the tracking error can converge to zero in a finite time.

Remark 9: Adaptive network-based fuzzy inference system (ANFIS) is a novel fuzzy inference structure, which combines

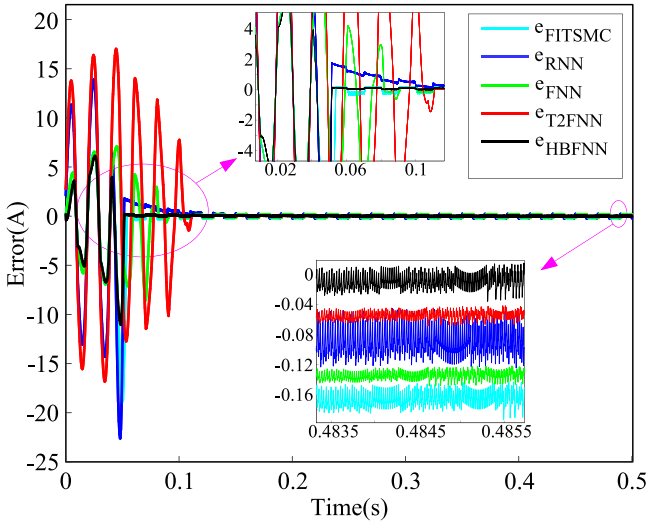

Fig. 12. Tracking error curves of different controllers.

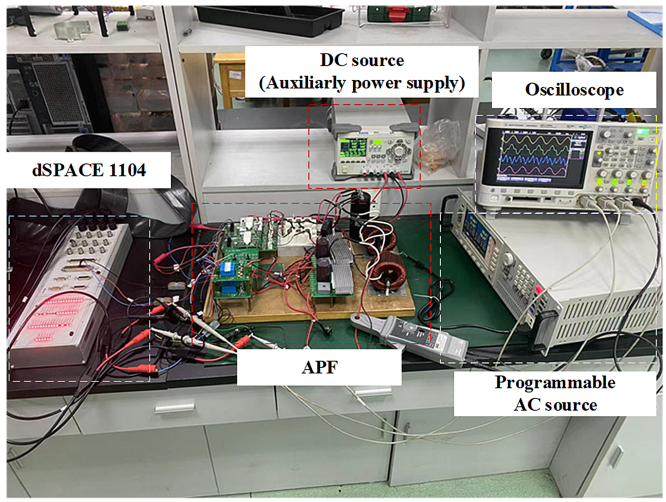

Fig. 13. Experimental platform.

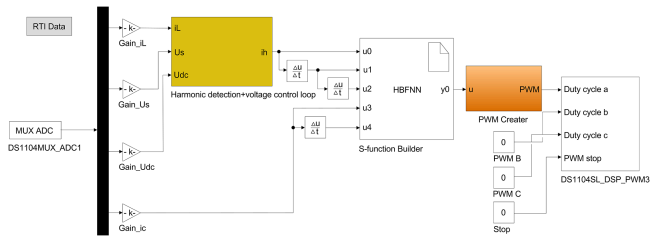

Fig. 14. Real-time simulation model.

fuzzy logic and NN. HBFNN and ANFIS both contain input layer, membership function layer, rule layer, and output layer. The main difference between HBFNN and ANFIS is hippocampus layer. Owing to hippocampus layer, HBFNN possesses better nonlinear representation capability than ANFIS, and it will not convert to ANFIS due to the difference from structure.

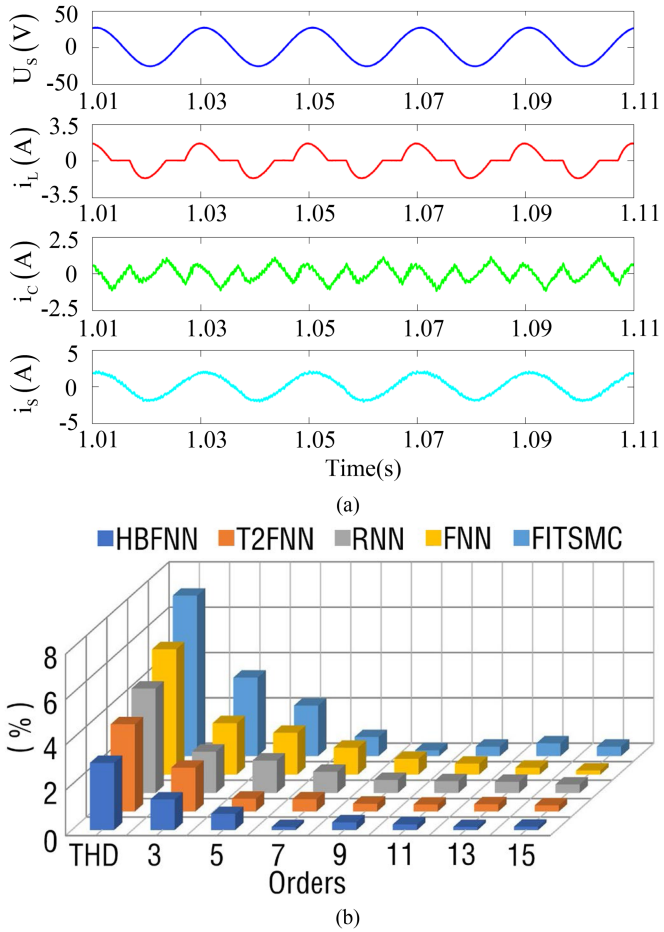

Fig. 15. Steady-state experimental results. (a) Experimental waveform. (b) THD of source current.

TABLE V
THD OF SOURCE-SIDE CURRENT UNDER DIFFERENT CONDITIONS

Case	HBFNN	T2FNN	RNN	FNN	FITSMC
Steady-state	2.96%	3.85%	4.61%	5.53%	7.08%
Loads decrease	3.24%	4.51%	5.01%	6.13%	7.36%
Loads increase	2.99%	4.37%	4.66%	5.65%	7.31%
Voltage increase	3.33%	4.65%	4.96%	6.10%	7.64%
Voltage decrease	3.56%	4.83%	5.30%	6.60%	8.15%
Voltage swell	3.40%	4.79%	5.04%	6.07%	8.02%
Voltage sag	3.63%	4.93%	5.26%	6.43%	8.61%

Remark 10: Recent studies show that, compared with conventional NNs, brain-like NNs have stronger generalization ability and learning ability, faster processing speed, stronger anti-interference ability, and more scientific information processing process [61], [62], [33]. However, the research of such brain-like NNs is extremely rare. Since the hippocampus tissue of human brain is responsible for human learning and memory tasks [36], [39], this article designs a novel HBFNN to learn

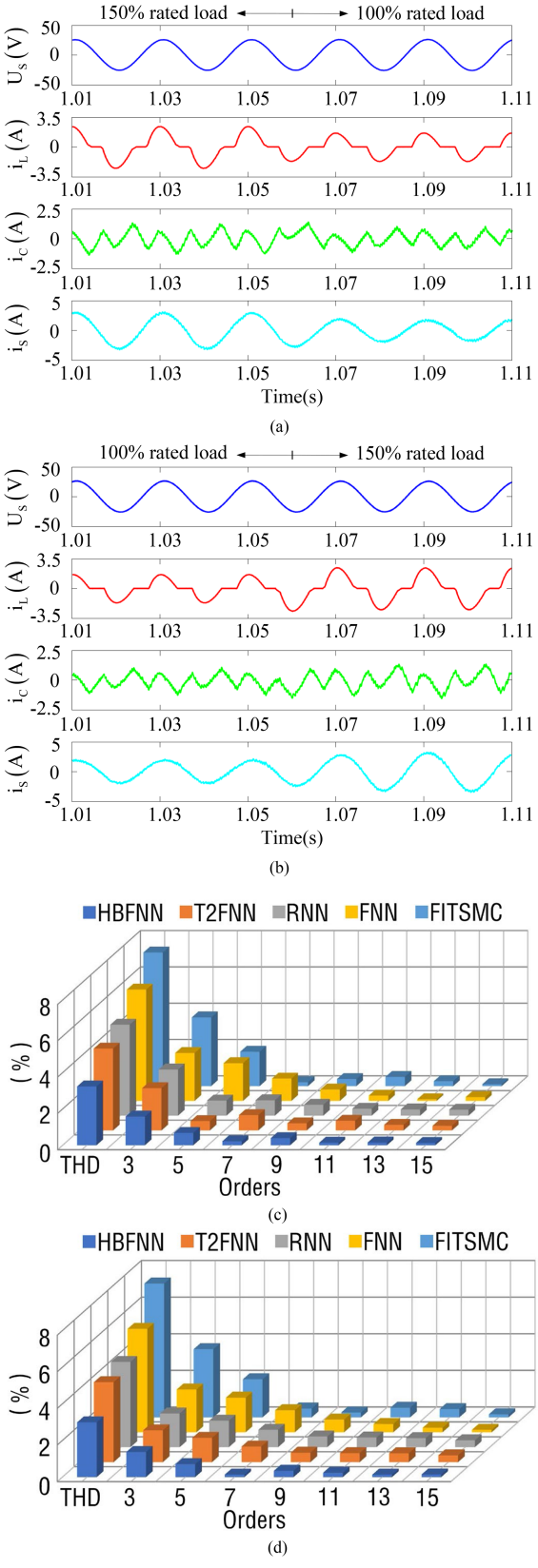

Fig. 16. Experimental waveform using the proposed HBFNN controller. (a) Load decrease. (b) Load increase. (c) Harmonic analysis of source current under load decrease. (d) harmonic analysis of source current under load increase.

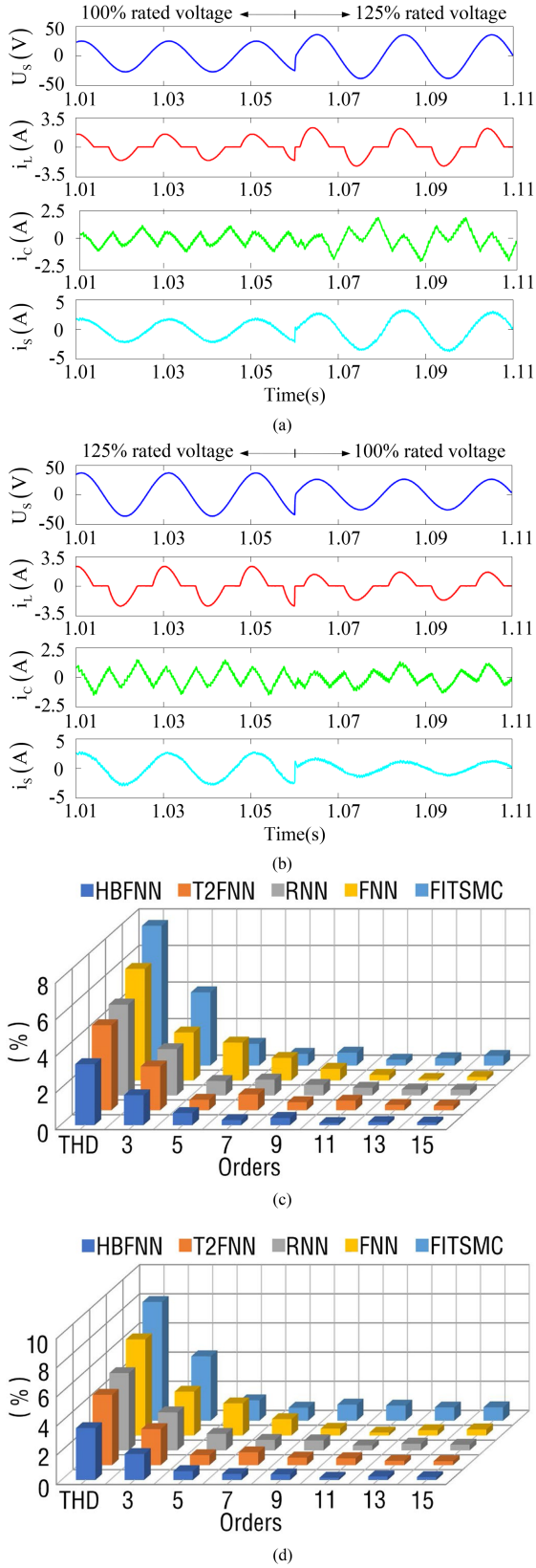

Fig. 17. Experimental waveform using the proposed HBFNN controller. (a) Voltage increase. (b) Voltage decrease. (c) Harmonic analysis of source current under voltage increase. (d) Harmonic analysis of source current under voltage decrease.

the SMC. Compared with the conventional RNN and FNN, the DG layer of the proposed HBFNN has a distinctive feature selection mechanism, which can filter the information in the network. Through a specific feature selection algorithm, important features in the network can be extracted for processing and unimportant features are not processed, thus improving the calculation and learning efficiency of the network, and enhancing control accuracy of system. In addition, conventional FNN does not have the recurrent feedback structure [41]. The experimental results show that the internal recurrent feedback structure of RNN can enhance the anti-interference ability of the network and the capability to process timing signals [43], [63]. Conventional RNN usually has an internal recurrent feedback structure [30], [43]. The proposed HBFNN has two recurrent feedback structures, one of which is the internal recurrent feedback structure of the CA3 layer, and the other of which is the external recurrent feedback structure from the CA1 layer to the EC layer. This double recurrent structure enables HBFNN to process time-varying input signals more efficiently and have stronger robustness. Figs. 15, 16, 17, and Table V in the experimental part of this article show that the THD of the proposed method is always lower than that of RNN and FNN under steady state and various interference environments, indicating that HBFNN has higher control accuracy and stronger anti-interference ability than RNN and FNN.

Remark 11: The FITSMC (i.e., $s = \dot{e} + \alpha e + \beta \int_0^t e^{p/q} d\tau$) consists of three parts, namely αe, $\dot{e}$, and $\beta \int_0^t e^{p/q} d\tau$. αe in FITSMC can reflect the tracking error of the control system in proportion. Therefore, once the tracking error occurs, the controller will take action immediately to reduce the tracking error and the rapidity of the control system is guaranteed. $\dot{e}$ in FITSMC can reflect the variation trend of tracking error, thereby reducing the phenomenon of large oscillation of tracking error curve and improving the dynamic characteristics. The function of $\beta \int_0^t e^{p/q} d\tau$ in FITSMC is to eliminate steady-state error and improve the control precision. In addition, compared with the conventional linear sliding surfaces [64], FITSMC can ensure that the tracking error converges to zero in a finite time.

VI. Conclusion

This article utilized an FITSMC method to realize current tracking control for APF. Unfortunately, owing to the existence of lumped uncertainty, its control effect will be significantly affected. Hence, considering the universal approximation and excellent properties of brain-like NNs, an innovate HBFNN was proposed and constructed according to the biological structure of the hippocampus. Consequently, a hybrid control strategy combining FITSMC and HBFNN was developed and applied to APF to achieve harmonic suppression. Meanwhile, the stability of the closed-loop system was proved strictly in accordance with Lyapunov stability criterion. Besides, a series of simulation and experimental results successfully validated the practicability and effectiveness of the proposed control scheme. Ultimately, the various three-dimensional bar charts and table data processed by comparative experiments further revealed the superiority and robustness of the proposed control scheme.

REFERENCES

[1] A. Cervone, T. Wei, and D. Dujic, "Stability analysis of input-series/output-parallel solid-state transformers equipped with second-order harmonic active power filters," *IEEE Trans. Power Electron.*, vol. 39, no. 4, pp. 4127–4138, Apr. 2024.

[2] M. Zhang, X. Sun, J. Teng, L. Qi, H. Shen, and X. Li, "Standing wave compensation based harmonic propagation mitigation for closed-loop distribution feeder," *IEEE Trans. Power Electron.*, to be published, doi: 10.1109/TPEL.2024.3432311.

[3] B. Yang, H. Li, L. Shan, L. Wei, and S. Lu, "A fundamental and harmonic frequencies decoupled control scheme to improve the output current quality of grid-forming inverters," *IEEE Trans. Power Electron.*, to be published, doi: 10.1109/TPEL.2024.3416469.

[4] S. Wang et al., "Harmonic resonance suppression with inductive power filtering method: Case study of large-scale photovoltaic plant in China," *IEEE Trans. Power Electron.*, vol. 38, no. 5, pp. 6444–6454, May 2023.

[5] J. Liu, J. Wang, and D. Chen, "Research on sliding mode and passivity based control strategy of active power filter," *Power Gener. Technol.*, vol. 44, no. 2, pp. 280–286, 2023.

[6] Z. Li, M. Ren, Z. Chen, G. Liu, and D. Feng, "A Bi-sliding mode PI control of DC-link voltage of three-phase three-wire shunt active power filter," *IEEE J. Emerg. Sel. Topics Power Electron.*, vol. 10, no. 6, pp. 7581–7588, Dec. 2022.

[7] B. L. G. Costa, V. D. Bacon, S. A. O. da Silva, and B. A. Angélico, "Tuning of a PI-MR controller based on differential evolution metaheuristic applied to the current control loop of a shunt-APF," *IEEE Trans. Ind. Electron.*, vol. 64, no. 6, pp. 4751–4761, Jun. 2017.

[8] G. Pandove and M. Singh, "Robust repetitive control design for a three-phase four wire shunt active power filter," *IEEE Trans. Ind. Informat.*, vol. 15, no. 5, pp. 2810–2818, May 2019.

[9] X. Cao, Q. Ge, J. Zhu, G. Kong, B. Zhang, and X. Wang, "Improved sliding mode traction control combined sliding mode disturbance observer strategy for high-speed maglev train," *IEEE Trans. Power Electron.*, vol. 38, no. 1, pp. 827–838, Jan. 2023.

[10] R. K. Jain, V. R. Barry, and H. K. V. Gadiraju, "An effective control strategy for single-phase single-stage PV grid-tied inverter under abnormal grid conditions," *IEEE J. Emerg. Sel. Topics Power Electron.*, vol. 12, no. 2, pp. 1249–1260, Apr. 2024.

[11] R. K. Jain, V. R. Barry, and G. H. K. Varma, "Power quality improvement for PV array reconfiguration based grid tied system," in *Proc. 11th Nat. Power Electron. Conf.*, 2023, pp. 1–6, doi: 10.1109/NPEC57805.2023.10384925.

[12] R. K. Jain, V. R. Barry, and H. K. V. Gadiraju, "Model-based design and sliding mode control approach for two-stage water pumping system with reduced sensors," *IEEE J. Emerg. Sel. Topics Power Electron.*, vol. 10, no. 4, pp. 3940–3949, Aug. 2022.

[13] T. Yang, Y. Deng, H. Li, Z. Sun, H. Cao, and Z. Wei, "Fast integral terminal sliding mode control with a novel disturbance observer based on iterative learning for speed control of PMSM," *ISA Trans.*, vol. 134, pp. 460–471, 2023, doi: 10.1016/j.isatra.2022.07.029.

[14] C.-Y. Chan, "Adaptive sliding-mode control of a novel buck-boost converter based on zeta converter," *IEEE Trans. Circuits Syst. II: Exp. Briefs*, vol. 69, no. 3, pp. 1307–1311, Mar. 2022.

[15] J. Wang, C. Yang, J. Xia, Z.-G. Wu, and H. Shen, "Observer-based sliding mode control for networked fuzzy singularly perturbed systems under weighted try-once-discard protocol," *IEEE Trans. Fuzzy Syst.*, vol. 30, no. 6, pp. 1889–1899, Jun. 2022.

[16] W. Xu et al., "Improved adaptive terminal sliding-mode reaching law for speed control of TPMLSM with disturbance observer," *IEEE Trans. Ind. Appl.*, vol. 59, no. 3, pp. 3210–3219, May/Jun. 2023.

[17] J. Wang, L. Zhao, and L. Yu, "Adaptive terminal sliding mode control for magnetic levitation systems with enhanced disturbance compensation," *IEEE Trans. Ind. Electron.*, vol. 68, no. 1, pp. 756–766, Jan. 2021.

[18] H. Wang, Q. Zhang, Z. Sun, X. Tang, and I.-M. Chen, "Continuous terminal sliding-mode control for FJR subject to matched/mismatched disturbances," *IEEE Trans. Cybern.*, vol. 52, no. 10, pp. 10479–10489, Oct. 2022.

[19] P. Ge, Y. Zhu, T. C. Green, and F. Teng, "Resilient secondary voltage control of islanded microgrids: An ESKBF-based distributed fast terminal sliding mode control approach," *IEEE Trans. Power Syst.*, vol. 36, no. 2, pp. 1059–1070, Mar. 2021.

[20] V. K. Tripathi, A. K. Kamath, L. Behera, N. K. Verma, and S. Nahavandi, "An adaptive fast terminal sliding-mode controller with power rate proportional reaching law for quadrotor position and altitude tracking," *IEEE Trans. Syst., Man, Cybern.: Syst.*, vol. 52, no. 6, pp. 3612–3625, Jun. 2022.

[21] P. Kumar, D. V. Bhaskar, R. K. Behera, and U. R. Muduli, "Continuous fast terminal sliding surface-based sensorless speed control of PMBLDCM drive," *IEEE Trans. Ind. Electron.*, vol. 70, no. 10, pp. 9786–9798, Oct. 2023.

[22] Z. Echreshavi, M. Farbood, and M. Shasadeghi, "Fuzzy event-triggered integral sliding mode control of nonlinear continuous-time systems," *IEEE Trans. Fuzzy Syst.*, vol. 30, no. 7, pp. 2347–2359, Jul. 2022.

[23] Z. Li, F. Wang, D. Ke, J. Li, and W. Zhang, "Robust continuous model predictive speed and current control for PMSM with adaptive integral sliding-mode approach," *IEEE Trans. Power Electron.*, vol. 36, no. 12, pp. 14398–14408, Dec. 2021.

[24] S. Kuppusamy and Y. H. Joo, "Memory-based integral sliding-mode control for T–S fuzzy systems with PMSM via disturbance observer," *IEEE Trans. Cybern.*, vol. 51, no. 5, pp. 2457–2465, May 2021.

[25] Y. Xu, S. Li, and J. Zou, "Integral sliding mode control based deadbeat predictive current control for PMSM drives with disturbance rejection," *IEEE Trans. Power Electron.*, vol. 37, no. 3, pp. 2845–2856, Mar. 2022.

[26] S. Lee and D. Chwa, "Dynamic image-based visual servoing of monocular camera mounted omnidirectional mobile robots considering actuators and target motion via fuzzy integral sliding mode control," *IEEE Trans. Fuzzy Syst.*, vol. 29, no. 7, pp. 2068–2076, Jul. 2021.

[27] V.-T. Do and S.-G. Lee, "Neural integral backstepping hierarchical sliding mode control for a ridable ballbot under uncertainties and input saturation," *IEEE Trans. Syst., Man, Cybern.: Syst.*, vol. 51, no. 11, pp. 7214–7227, Nov. 2021.

[28] S. C. Yogi, V. K. Tripathi, and L. Behera, "Adaptive integral sliding mode control using fully connected recurrent neural network for position and attitude control of quadrotor," *IEEE Trans. Neural Netw. Learn. Syst.*, vol. 32, no. 12, pp. 5595–5609, Dec. 2021.

[29] W. Dai, L. Zhang, J. Fu, T. Chai, and X. Ma, "Dual-rate adaptive optimal tracking control for dense medium separation process using neural networks," *IEEE Trans. Neural Netw. Learn. Syst.*, vol. 32, no. 9, pp. 4202–4216, Sep. 2021.

[30] J. Fei and H. Wang, "Experimental investigation of recurrent neural network fractional-order sliding mode control of active power filter," *IEEE Trans. Circuits Syst. II: Exp. Briefs*, vol. 67, no. 11, pp. 2522–2526, Nov. 2020.

[31] F. Baghbani, M. R. Akbarzadeh-T, M. B. Naghibi-Sistani, and A. Akbarzadeh, "Emotional neural networks with universal approximation property for stable direct adaptive nonlinear control systems," *Eng. Appl. Artif. Intell.*, vol. 89, 2020, Art. no. 103447.

[32] C. Xu, C. Wang, J. Jiang, J. Sun, and H. Lin, "Memristive circuit implementation of context-dependent emotional learning network and its application in multitask," *IEEE Trans. Comput.-Aided Des. Integr. Circuits Syst.*, vol. 41, no. 9, pp. 3052–3065, Sep. 2022.

[33] H. Zhang, C. Gang, C. Xu, G. Gong, and H. Lu, "Brain-inspired spiking neural network using superconducting devices," *IEEE Trans. Emerg. Topics Comput. Intell.*, vol. 7, no. 1, pp. 271–277, Feb. 2023.

[34] C. H. Tan, H. Tang, E. Y. Cheu, and J. Hu, "A computationally efficient associative memory model of hippocampus CA3 by spiking neurons," in *Proc. Int. Joint Conf. Neural Netw.*, 2013, pp. 1–8.

[35] T. W. Berger et al., "A hippocampal cognitive prosthesis: Multi-input, multi-output nonlinear modeling and VLSI implementation," *IEEE Trans. Neural Syst. Rehabil. Eng.*, vol. 20, no. 2, pp. 198–211, Mar. 2012.

[36] A. A. Dibazar, A. Yousefi, and T. W. Berger, "Multi-layer spike-in spike-out representation of Hippocampus circuitry," in *Proc. 6th Int. IEEE/EMBS Conf. Neural Eng.*, 2013, pp. 613–616.

[37] F. Ren, X. Wang, and Z. Zeng, "Improved fixed-time stabilization of fuzzy neural networks with distributed delay via adaptive sliding mode control," *IEEE Trans. Fuzzy Syst.*, vol. 31, no. 6, pp. 2029–2043, Jun. 2023.

[38] J. Wang, W. Luo, J. Liu, and L. Wu, "Adaptive type-2 FNN-based dynamic sliding mode control of DC–DC boost converters," *IEEE Trans. Syst., Man, Cybern.: Syst.*, vol. 51, no. 4, pp. 2246–2257, Apr. 2021.

[39] C.-M. Lin, D.-H. Pham, and T.-T. Huynh, "Encryption and decryption of audio signal and image secure communications using chaotic system synchronization control by TSK fuzzy brain emotional learning controllers," *IEEE Trans. Cybern.*, vol. 52, no. 12, pp. 13684–13698, Dec. 2022.

[40] S. Hou and J. Fei, "Adaptive fuzzy backstepping control of three-phase active power filter," *Control Eng. Pract.*, vol. 45, pp. 12–21, 2015, doi: 10.1016/j.conengprac.2015.08.005.

[41] S. Hou, J. Fei, C. Chen, and Y. Chu, "Finite-time adaptive fuzzy-neural-network control of active power filter," *IEEE Trans. Power Electron.*, vol. 34, no. 10, pp. 10298–10313, Oct. 2019.

[42] Y. Shtessel, C. Edwards, L. Fridman, and A. Levant, *Sliding Mode Control and Observation (Control Engineering)*. Berlin, Germany: Springer-Verlag, 2014.

[43] J. Fei and Y. Chen, "Dynamic terminal sliding-mode control for single-phase active power filter using new feedback recurrent neural network," *IEEE Trans. Power Electron.*, vol. 35, no. 9, pp. 9904–9922, Sep. 2020, doi: 10.1109/TPEL.2020.2974470.
[44] Y. Feng, M. Zhou, Q. Han, F. Han, Z. Cao, and S. Ding, "Integral-type sliding-mode control for a class of mechatronic systems with gain adaptation," *IEEE Trans. Ind. Informat.*, vol. 16, no. 8, pp. 5357–5368, Aug. 2020.
[45] L. Yipeng, L. Jie, Z. Fengge, and Z. Ming, "Fuzzy sliding mode control of magnetic levitation system of controllable excitation linear synchronous motor," *IEEE Trans. Ind. Appl.*, vol. 56, no. 5, pp. 5585–5592, Sep./Oct. 2020.
[46] R.-Q. Dong, A.-G. Wu, Y. Zhang, G.-R. Duan, and J. Huang, "Antiunwinding sliding mode control for rigid spacecraft based on modified rodrigues parameters," *IEEE Trans. Aerosp. Electron. Syst.*, vol. 59, no. 3, pp. 2579–2592, Jun. 2023.
[47] F.-J. Lin, C.-I. Chen, G.-D. Xiao, and P.-R. Chen, "Voltage stabilization control for microgrid with asymmetric membership function-based wavelet petri fuzzy neural network," *IEEE Trans. Smart Grid*, vol. 12, no. 5, pp. 3731–3741, Sep. 2021.
[48] S. Tong, Y. Li, and Y. Liu, "Observer-based adaptive neural networks control for large-scale interconnected systems with nonconstant control gains," *IEEE Trans. Neural Netw. Learn. Syst.*, vol. 32, no. 4, pp. 1575–1585, Apr. 2021, doi: 10.1109/TNNLS.2020.2985417.
[49] F. J. Lin, S. G. Chen, and C.-W. Hsu, "Intelligent backstepping control using recurrent feature selection fuzzy neural network for synchronous reluctance motor position servo drive system," *IEEE Trans. Fuzzy Syst.*, vol. 27, no. 3, pp. 413–427, Mar. 2019.
[50] J. Na, Y. Huang, X. Wu, Y.-J. Liu, Y. Li, and G. Li, "Active suspension control of quarter-car system with experimental validation," *IEEE Trans. Syst., Man, Cybern.: Syst.*, vol. 52, no. 8, pp. 4714–4726, Aug. 2022.
[51] S. Echalih et al., "Nonlinear control design and stability analysis of single phase half bridge interleaved buck shunt active power filter," *IEEE Trans. Circuits Syst. I: Reg. Papers*, vol. 69, no. 5, pp. 2117–2128, May 2022.
[52] A. D. Kumar, J. Gupta, and B. Singh, "A bridgeless semi-quadratic gain high power factor AC-DC converter based LEVs charging solution," *IEEE Trans. Ind. Appl.*, vol. 59, no. 5, pp. 6324–6335, Sep./Oct. 2023.
[53] O. C. da Silva Filho, F. L. Tofoli, L. H. S. C. Barreto, and D. de Souza Oliveira, "Single-phase isolated AC–AC symmetrical full-bridge converter," *IEEE J. Emerg. Sel. Topics Power Electron.*, vol. 10, no. 1, pp. 846–855, Feb. 2022.
[54] S. Lian et al., "Adaptive attitude control of a quadrotor using fast nonsingular terminal sliding mode," *IEEE Trans. Ind. Electron.*, vol. 69, no. 2, pp. 1597–1607, Feb. 2022.
[55] O. Mofid and S. Mobayen, "Adaptive finite-time backstepping global sliding mode tracker of quad-rotor UAVs under model uncertainty, wind perturbation, and input saturation," *IEEE Trans. Aerosp. Electron. Syst.*, vol. 58, no. 1, pp. 140–151, Feb. 2022.
[56] S. Hou, Y. Chu, and J. Fei, "Adaptive type-2 fuzzy neural network inherited terminal sliding mode control for power quality improvement," *IEEE Trans. Ind. Informat.*, vol. 17, no. 11, pp. 7564–7574, Nov. 2021.
[57] Z. Wang et al., *Harmonic Suppression and Reactive Power Compensation*. Beijing, China: Mach. Press, 2005, pp. 280–284.
[58] S. K. Khadem, M. Basu, and M. F. Conlon, "Harmonic power compensation capacity of shunt active power filter and its relationship with design parameters," *IET Power Electron.*, vol. 7, no. 2, pp. 418–430, Feb. 2013.
[59] X. Chen et al., "Fuzzy-based controller synthesis and optimization for underactuated mechanical systems with nonholonomic servo constraints," *IEEE Trans. Fuzzy Syst.*, vol. 30, no. 10, pp. 4152–4164, Oct. 2022.
[60] L. Shanmugam and Y. H. Joo, "Design of interval type-2 fuzzy-based sampled-data controller for nonlinear systems using novel fuzzy Lyapunov functional and its application to PMSM," *IEEE Trans. Syst., Man, Cybern.: Syst.*, vol. 51, no. 1, pp. 542–551, Jan. 2021.
[61] E. Lotfi and M. R. Akbarzadeh-T, "Practical emotional neural networks," *Neural Netw.*, vol. 59, pp. 61–72, 2014, doi: 10.1016/j.neunet.2014.06.012.
[62] H. Zhou et al., "Bionic dual-loop emotional learning circuit and its application in radiation early warning monitoring," *IEEE Trans. Cogn. Devlop. Syst.*, vol. 15, no. 3, pp. 1196–1208, Sep. 2023.
[63] S. Cai and V. K. N. Lau, "Remote state estimation of nonlinear systems over fading channels via recurrent neural networks," *IEEE Trans. Neural Netw. Learn. Syst.*, vol. 33, no. 8, pp. 3908–3922, Aug. 2022.
[64] H. Huang, G. Tang, H. Chen, L. Han, and D. Xie, "Dynamic modeling and vibration suppression for two-link underwater flexible manipulators," *IEEE Access*, vol. 10, pp. 40181–40196, 2022, doi: 10.1109/ACCESS.2022.3164706.

Shixi Hou (Member, IEEE) received the B.S. degree in automation and the Ph.D. degree in electrical engineering from Hohai University, Nanjing, China, in 2011 and 2016, respectively.

He is currently an Associate Professor with Hohai University. His research interests include power electronics, adaptive control, nonlinear control, and intelligent control.

Zhenyu Qiu received the B.S. degree in automation in 2022 from Hohai University, Nanjing, China, where he is currently working toward the M.S. degree in control engineering.

His research interests include neural network control, adaptive control, sliding-mode control, artificial intelligence.

Yundi Chu received the B.S., M.S., and Ph.D. degrees in electrical engineering from Hohai University, Nanjing, China, in 2013, 2016, and 2019, respectively.

She is currently an Associate Professor with Hohai University. Her research interests include power electronics, adaptive control, intelligent control, nonlinear control, etc.

Jie Gao received the B.S. degree in automation in 2021 from Hohai University, Nanjing, China, where he is currently working toward the M.S. degree in control engineering.

His research interests include fault protection, deep learning, and neural networks.

Juntao Fei (Senior Member, IEEE) received the B.S. degree from the Hefei University of Technology, Hefei, China, in 1991, the M.S. degree from the University of Science and Technology of China, Hefei, China, in 1998, both in electrical engineering, and the M.S. and Ph.D. degrees in mechanical engineering from The University of Akron, Akron, OH, USA, in 2003 and 2007, respectively.

He was a Visiting Scholar with the University of Virginia, Charlottesville, VA, USA, from 2002 to 2003. He was a Postdoctoral Research Fellow and an Assistant Professor with the University of Louisiana, Lafayette, LA, USA, from 2007 to 2009. He is currently a Professor with Hohai University, Nanjing, China. His research interests include adaptive control, nonlinear control, intelligent control, dynamics and control of MEMS, and smart materials and structures.